공학석사 학위논문

Finite Element Analysis of Ultimate Strength of Flexible Risers Subject to Axial Compression Using Simplified Model

축 압축력을 받는 유연식 라이저의 극한 강도의 간략화 모델을 이용한 유한 요소 해석

2017 년 08 월

서울대학교 대학원

조선해양공학과

유 동 현

Finite Element Analysis of Ultimate Strength of Flexible Risers Subject to Axial Compression Using Simplified Model

지도 교수 장 범 선

이 논문을 공학석사 학위논문으로 제출함

2017 년 8 월

서울대학교 대학원
조선해양공학과
유 동 현

유동현의 공학석사 학위논문을 인준함

2017 년 8 월

위 원 장 _____ 신 종 계 _____ (인)

부위원장 _____ 장 범 선 _____ (인)

위 원 _____ 노 명 일 _____ (인)

Abstract

Finite Element Analysis of Ultimate Strength of Flexible Risers Subject to Axial Compression Using Simplified Model

Yoo Donghyun

Department of Naval Architecture and Ocean Engineering

The Graduate School

Seoul National University

Flexible risers are pipes connecting the offshore platform to the subsea flow line and transporting gas and oil. Flexible risers can encounter many uncertain factors during their installation and operation process. Especially, during installation process, due to the

pressure unbalance, flexible risers can be subject to axial compression, which is an undesirable force. Axial compression can result in failure modes such as radial buckling. Therefore, it is very necessary to analysis failure modes and to evaluate the ultimate strength of flexible risers. Ultimate strength assessment of flexible risers is very complicated and time-consuming. This is because it includes many difficult points such as material nonlinearity, large deformation, and nonlinear contact mechanism. Also, it is difficult to understand structural behaviors under various loads. This paper introduces practical and stable methods for ultimate strength assessment using simplified FE models. In particular, numerical methods are provided to increase convergence of nonlinear analysis. In addition, the effects of ovalizations and external pressure are examined.

Keywords : flexible risers, ultimate strength assessment, failure mode, nonlinear FE analysis, simplified FE models

Student Number : 2015-22866

Contents

List of Figures

List of Tables

1. Introduction

1.1. Introduction to Flexible Riser

The offshore plant consists of topside, platform and subsea parts. A riser is a pipe connecting the offshore platform to the subsea flow line and transporting gas and oil. A flexible riser is a kind of riser and is used for dynamic applications that receive various loads cyclically. It has a high axial stiffness and a very low bending stiffness. The bending stiffness of the flexible riser is about 1/25 of that of Steel Catenary Riser. This is because the flexible riser consists of layers with different materials and shapes.

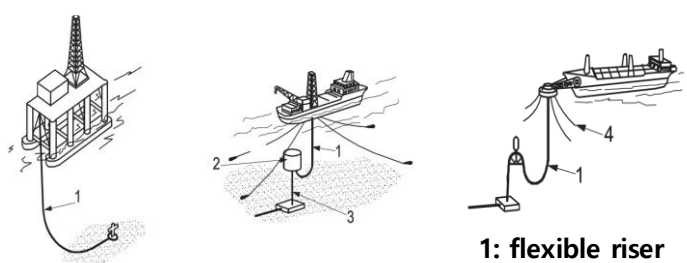

Fig. 1 The concept of flexible riser

The flexible riser consists of metal and polymer layers. The model used in this study has an inner diameter of 2.5-inch and consists of eight layers. From the inside, carcass, pressure sheath, pressure armor, a pair of anti-friction tapes, a pair of tensile armor layers and fabric tape are laid like Fig. 2.

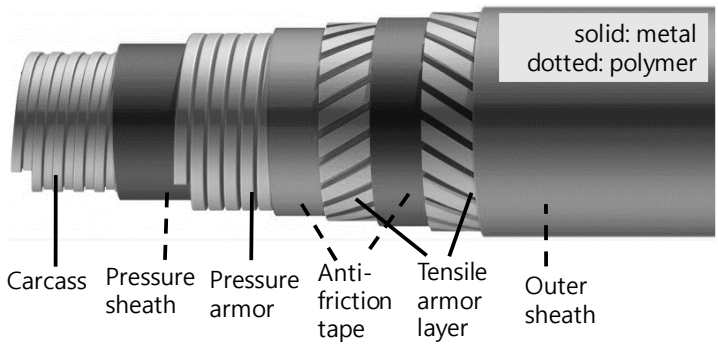

Fig. 2 Composition of flexible riser

Each layer has its own function. Carcass, the innermost layer, enables the flexible riser to withstand strong external pressure. However, since the internal fluid passes inside and outside of the carcass, this layer cannot withstand the internal pressure. The pressure armor serves to withstand both internal pressure and external pressure. The carcass and pressure armor have a unique cross-sectional shape, so the radial stiffness is large but the axial stiffness is very small. They are like shower hoses. Fig. 3 shows the complex cross section of carcass and pressure armor.

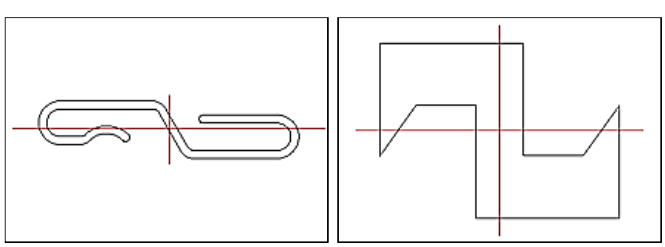

Fig. 3 Cross section of carcass (L) and pressure armor (R)

A pair of tensile armor layers has a large axial stiffness and consists of helical tendons. In addition, in order to balance about torque, a pair of layers is always wound in the opposite direction. Anti-friction tapes reduce the friction between metal layers. In addition, pressure sheath and fabric tape play roles of insulation and watertight simultaneously. Table 1 lists the function of all layers.

Table 1 Function of layers of flexible riser

Layer	Function
Carcass	Pressure resistance
Pressure armor	Pressure resistance
Tensile armor layers	Axial resistance
Pressure sheath	Polymer barrier, thermal insulation
Outer sheath	Polymer barrier, thermal insulation
Anti-friction tapes	Decrease friction between metal

1.2. Research Background

A flexible riser is subject to various and unpredictable loads during the installation and operation processes. For example, the loads include gravity and buoyancy of itself, loads due to dynamic motions of offshore platforms, and nonlinear loads due to interaction with soil at Touch Down Zone (TDZ).

In particular, the maximum net pressure is imposed during installation because there is no internal fluid, but the large

hydrostatic pressure acting on the outside of flexible riser. The TDZ experiences the largest pressure unbalance and this can cause axial compression, an 'undesirable force' of the flexible riser. As shown in Fig. 4, when the flexible riser receives external pressure, it tends to elongate due to the Poisson effect. However, because of the friction with the seabed, one end becomes fixed and large reaction force applies to TDZ. This reaction force acts as axial compression. Since the flexible riser is not designed to withstand axial compressive forces well, relatively small loads can cause axial failure. A typical failure mode caused by the axial compression is radial buckling of tensile armor layers.

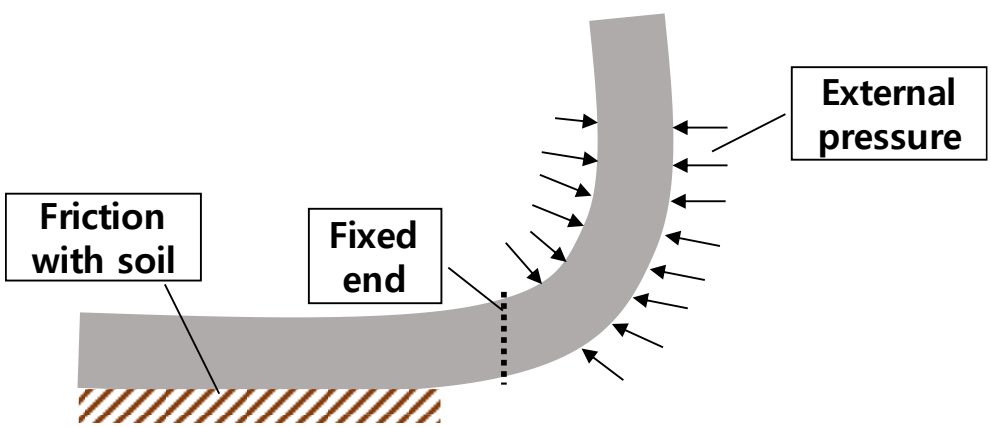

Fig. 4 Occurrence of axial force at TDZ

Literally, radial buckling is a buckling phenomenon of tendons in radial direction. This failure mode was first discovered in 1989, when the flexible riser was first used. As the tendons receive an

axial compression, they can deform perpendicular to the force. However, since metal layer inside the tendons supports them, the tendons cannot deform inward. In addition, the friction with the adjacent layers also suppresses the deformation in the circumferential direction. Therefore, the only direction in which the tendons can deform is the outward direction. The above explanation is summarized in Fig. 5.

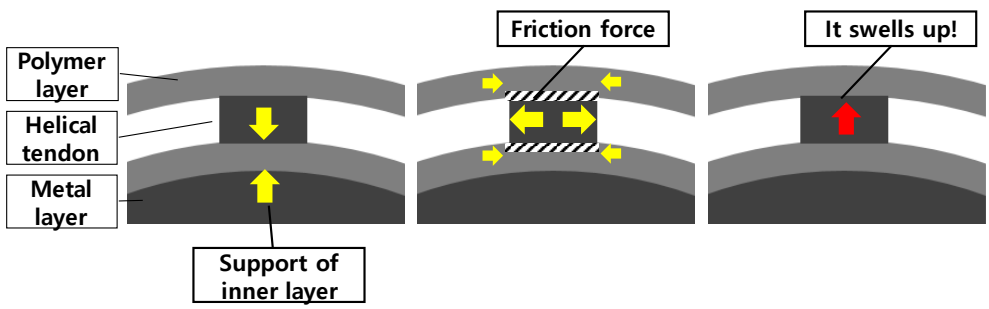

Fig. 5 Deformation of tendon due to axial compression

In other words, when the tendons are subject to axial compression, they expand in the radial direction. Of course, the outer polymer layers of the tendon (in this model, fabric tape and anti-friction tape) can delay the expansion of the tendons. However, the expansion of the tendons gives contact pressure to the tape, which gradually increases the stress of the tape. If this stress exceeds the yield strength of the tape, the tape will lose its capacity and the tendons will swell up quickly. This failure is also referred to

as a ‘bird-caging’ phenomenon because it is like a birdcage after its appearance. The Fig. 6 shows the failure modes of radial buckling.

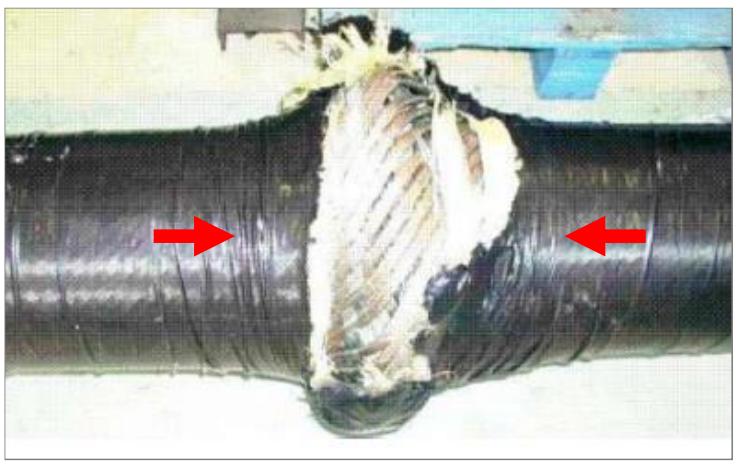

Fig. 6 Radial buckling failure mode

In this study, FE models of flexible riser are created using ANSYS Mechanical which is a commercial software, and nonlinear analyses are performed for ultimate strength due to axial compression. According to MCS Kenny's data (Fig. 7), the proportion of TDZ damage, bird caging, and armor wire failure in the accident (failure mode) of the flexible riser was about 12%. Failure modes of the tensile armor can cause serious problems such as internal fluid leakage and can cause enormous damage both economically and environmentally. Therefore, failure mode and ultimate strength analysis are essential when designing flexible

risers.

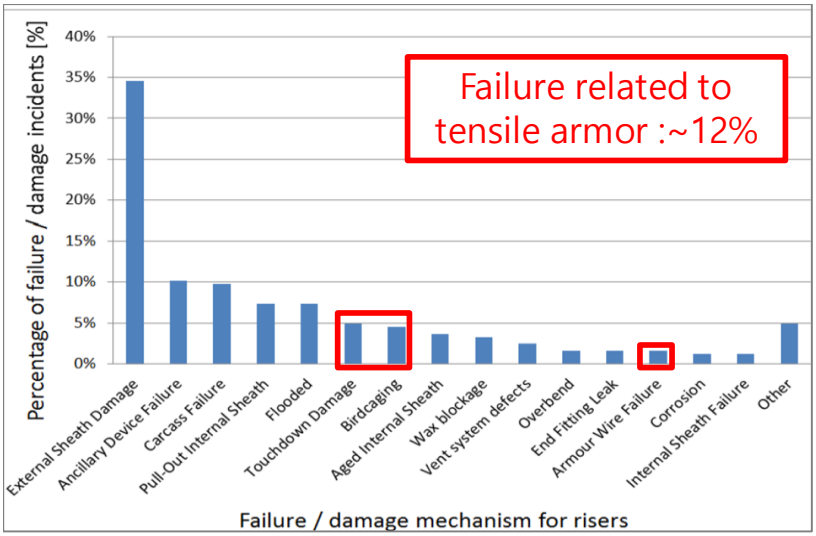

Fig. 7 Various failure/damage mechanism of risers, NTNU (2014)

In this study, the model of Witz (1996) is used but there is a slight difference from the usual flexible riser. The usual flexible riser has a thick outer sheath as the outermost layer, but this model instead includes a thin fabric tape. This is because the model of Witz (1996) was designed for simple stiffness test. However, this incomplete model is useful for evaluating the ultimate compressive strength. This is because the failure mode of the tensile armor occurs easily in the flooded annulus state where the outer sheath is damaged. Therefore, the ultimate strength evaluation can be performed with the model of Witz (1996).

1.3. Previous Studies

In the early days when flexible risers were used, many analytical methods were developed. Feret and Bournazel (1987) formulated governing equations for the behavior of flexible pipes under axisymmetric loads and evaluated the stresses in tensile armor layers on the basis of a simplified solution for the helical tendons. However, the results are not valid when the layers are not in contact. A similar analytical model was provided by McNamara and Harte (1992).

After that, many experiments were conducted to examine the structural behaviors of flexible risers. Witz (1996) examined axial, torsional, and bending stiffness. The experiments of Witz (1996) have been used as reference for many studies. However, there is definite time and cost limitation in such an experimental method.

Again, there were many analytical methods. Kebadze (2002) also investigated the behavior of flexible pipes under axisymmetric loads, but with respect to various applications of kinematic models for each layer. The research proposed the use of the kinematics of the thin tube for isotropic layers. After that, Bahtui et. al (2009) described the behavior of flexible risers subject to axisymmetric

loads and bending moments in an analytical way. This method used the principle of virtual work. The analytical method consumed less time and cost, but it was based on many assumptions, so the accuracy was low and only elastic analyses were available.

Numerical studies have been developed since then. Sousa (2009) proposed a 3D FE model. In this study, equivalent orthotropic shells were proposed to replace carcass and pressure armor having complex cross-sections. Likewise, elastic analyses were performed.

In addition, many studies have been conducted on the ultimate strength evaluation. Sousa (2012) performed ultimate strength analysis. However, in this study, an 8-layered model was used like Fig. 8. This model involved many interactions between multiple layers. Therefore, the convergence was very poor and the accuracy was problematic.

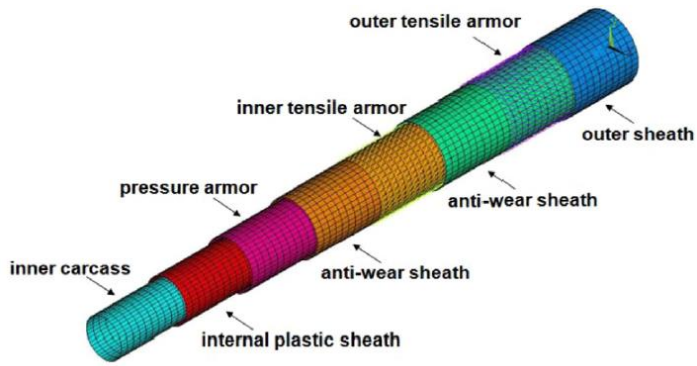

Fig. 8 The 8-layered model of Saevik (2012)

On the other hand, Vaz (2011) investigated various failure modes about axial compression. It proposed a FE model consisting of two beams, a cylinder face and a spring element like Fig. 9 (a). However, since the inner layers were not considered, the influence of the pressure could not be considered. After that, Saevik (2012) constructed the FE model with a beam, a face, and spring elements like Fig. 9 (b). This model also could not consider the influence of the pressure, did not include the interaction between layers, and was only available for elastic analyses.

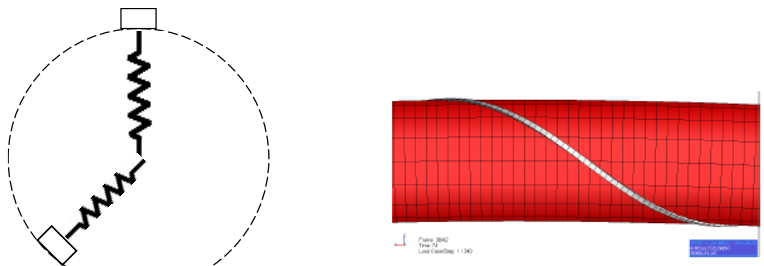

(a) (b)

Fig. 9 Simplified FE models of (a) Vaz (2011) and (b) Saevik (2012)

In this study, a 5−layered model is proposed which can reduce the computation time compared to the 8−layered model of Sousa (2012). An equivalent layer is conceived to replace the layers which are less related to the failure modes. As a result, the number of elements can be reduced for by 69%. In addition, this model can include interaction between tensile armor and inner layers and plastic deformation. The 5−layered model is proposed to overcome the shortcomings of models of Vaz (2011) and Saevik (2012).

1.4. Research Objective

This study proposes a practical numerical method for the ultimate strength analysis of a flexible riser. The FE model is created using commercial software ANSYS Mechanical (R.15.0) The ultimate

strength analysis includes various nonlinearities such as large deformation, material nonlinearity, and contact nonlinearity like Fig. 10. Thus, the FE model is not technically convergent, because of complex cross-sectional shapes and materials, and contact between multiple layers.

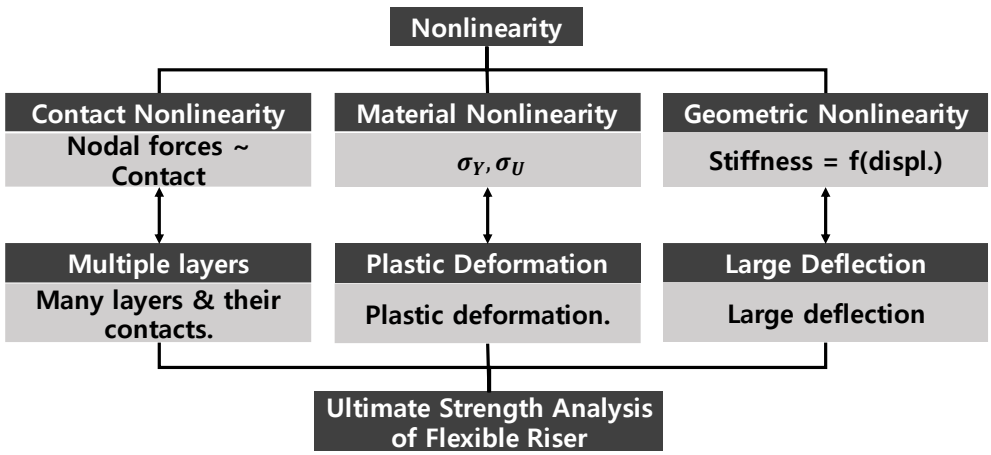

Fig. 10 Three nonlinearities used in analysis of flexible riser

Therefore, this paper proposes a technically stable FE model through three types of simplification.

- Simplification of geometry.
- Isotropic assumption
- Simplification of composition

First, the section shape is simplified. The most problematic layers are carcass and pressure armor with complex cross-sectional shapes. Sousa (2005) proposed a method of replacing a layer

having a complex cross section with an equivalent orthotropic layer. Equivalent layers can greatly simplify calculations and improve analytical convergence.

Second, we assume that the tape is an isotropic layer. Tape is orthotropic because it has different elastic modulus in the axial and transverse direction. However, when the tape is modeled as an orthotropic layer, the convergence become worse. Therefore, this study assumes it isotropic layer. An elastic analysis verifies the accuracy deterioration of this assumption is negligible. Through the above two steps, an ‘8-layered model’ is created.

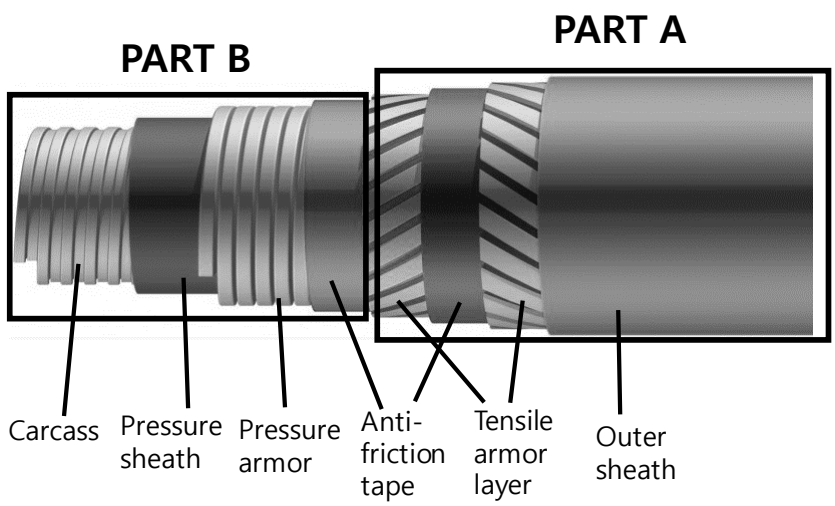

Fig. 11 Division of layers for simplification of model

Finally, the composition of model is simplified. Since the analysis of ultimate strength still includes complex interactions between

layers and large deformation, the convergence of analysis with the 8-layered model is very poor. Depending on its contribution to ultimate compressive strength, all layers can be divided into important layers (part A) and less important layers (part B) like Fig. 11. Then the layers of part B are replaced with one equivalent layer. A condition that must be satisfied here is that the equivalent layer should show the same structural behaviors with the layers of part B for axisymmetric loads and bending moment. In this simplification process, material properties and geometric information of the equivalent layer are determined using an analytical method. This model is named a '5-layered model'.

The 8-layered and 5-layered models are verified through elastic analyses for axial and bending stiffeness. The results of axial tension test and bending test are compared with those of Witz (1996) and Bahtui et. al (2009).

In addition, ultimate compressive strength is evaluated by nonlinear FE analysis. Likewise, the results are compared with the analytical methods of Saevik (2012). Moreover, the effects of ovalization and external pressure are examined.

This paper proceeds in the following order. First, material properties and geometric information of a 2.5-inch flexible riser is

represented. Next, a series of processes for constructing the FE model is described. It also explains how to determine the equivalent layer introduced to simplify the composition of model. Then axial/bending stiffness are calculated by performing elastic analysis based on the FE model, and the validity of the model is verified by comparing with the results of the reference method. Finally, the ultimate compressive strength analysis is performed and the results are compared with the analytical formulas. The results are discussed.

2. Analytical Method

2.1. Elastic stiffness of flexible riser

2.1.1. Behavior about axisymmetric loads

Bahtui et. al (2009) proposed an analytical method for the structural behavior of the flexible riser in the elastic region. In this study, analytical method is very useful because verification of numerical method, determination of penetration tolerance between elements and determination of EQP are based on the analytical method.

- Verification of numerical method

- Determination of penetration tolerance of shell elements
- Determination of equivalent pressure layer (EQP)

Bahtui et. al (2009) classified all layers of the flexible riser into isotropic cylinders, orthotropic cylinders, and helical tendons depending on the material and shape. The stiffness equations of each type were constructed from the principle of virtual work and internal energy.

(1) Isotropic cylinder

Isotropic cylinders include tape and sheath. In this case, the stiffness equation can be written as below. Each row represents axial, torsion, bending about the x−axis and y−axis, and radial stiffness equation.

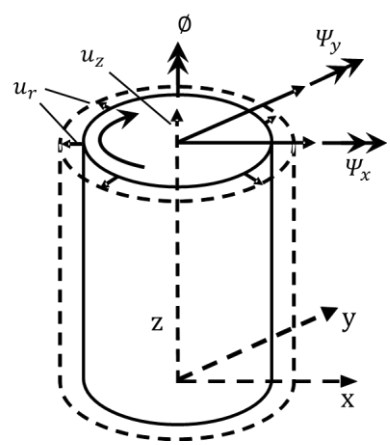

Fig. 12 Displacements about various loads

$$\frac{1}{1-\nu^2}\begin{bmatrix} AE & 0 & 0 & 0 & \nu AE \\ 0 & EI_z\frac{1}{2}(1-\nu) & 0 & 0 & 0 \\ 0 & 0 & EI_x & 0 & 0 \\ 0 & 0 & 0 & EI_y & 0 \\ \nu AE & 0 & 0 & 0 & AE \end{bmatrix}\begin{pmatrix} \frac{\Delta u_z}{L} \\ \frac{\Delta \varnothing}{L} \\ \frac{\Delta \Psi_x}{L} \\ \frac{\Delta \Psi_y}{L} \\ \frac{\Delta u_r}{R} \end{pmatrix} = \begin{pmatrix} N+\pi R^2 \Delta P \\ T \\ M_x \\ M_y \\ 2\pi R^2 \Delta P \end{pmatrix} \quad (1)$$

where, Δu_z, $\Delta\varnothing$, $\Delta\Psi_x$, $\Delta\Psi_y$ and Δu_r are axial displacement, axial rotation, the rotations about the normal/binormal directions, and the radial displacement respectively like Fig. 12. L is the length of pipe and R is the mean radius of the layer. In addition, N, T, M_x, M_y and Δp are the axial force, the axial torque, the moment about the normal direction, the moment about the bi-normal direction, and the radial pressure respectively. A, E, ν, $\mathrm{I_x}$, $\mathrm{I_y}$, and $\mathrm{I_z}$ are sectional area, elastic modulus, Poisson ratio of each layer, the second moment about x and y axes, and torsional moment.

(2) Orthotropic cylinder

Carcass and pressure armor correspond to this. The stiffness equation of the orthotropic cylindrical layer can be written as below.

$$\begin{bmatrix} AE_{S_1} & 0 & 0 & 0 & 0 \\ 0 & G_{S_{12}} I_z & 0 & 0 & 0 \\ 0 & 0 & E_{S_1} I_x & 0 & 0 \\ 0 & 0 & 0 & E_{S_1} I_y & 0 \\ 0 & 0 & 0 & 0 & AE_{S_2} \end{bmatrix}\begin{pmatrix} \frac{\Delta u_z}{L} \\ \frac{\Delta \varnothing}{L} \\ \frac{\Delta \Psi_x}{L} \\ \frac{\Delta \Psi_y}{L} \\ \frac{\Delta u_r}{R} \end{pmatrix} = \begin{pmatrix} N+\pi R^2 \Delta P \\ T \\ M_x \\ M_y \\ 2\pi R^2 \Delta P \end{pmatrix} \quad (2)$$

where, the subscript 's' means shell, and '1' and '2' mean the axial and circumferential directions. E_z is the axial stiffness of orthotropic layer, and almost zero.

(3) Helical tendon

A pair of tensile armor corresponds to this case. Unlike other layers, the helical tendon has a slip/stick state depending on the curvature.

The stiffness equation of the layer composed of helical tendon in the slip state can be written as follows. A detailed description of the slip / stick status will be made later.

$$\begin{bmatrix} cos^3\alpha & R\,cos^2\alpha\,sin\alpha & 0 & 0 & sin^2\alpha\,cos\alpha \\ R\,cos^2\alpha\,sin\alpha & R^2\,sin^2\alpha\,cos\alpha & 0 & 0 & R\,sin^3\alpha \\ 0 & 0 & \frac{1}{2}R^2\,cos^3\alpha & 0 & 0 \\ 0 & 0 & 0 & \frac{1}{2}R^2\,cos^3\alpha & 0 \\ sin^2\alpha\,cos\alpha & R\,sin^3\alpha & 0 & 0 & sin^3\alpha\,tan\alpha \end{bmatrix} \begin{pmatrix} \frac{\Delta u_z}{L} \\ \frac{\Delta\varnothing}{L} \\ \frac{\Delta\Psi_x}{L} \\ \frac{\Delta\Psi_y}{L} \\ \frac{\Delta r}{R} \end{pmatrix} =$$

$$\frac{1}{nEA}\begin{pmatrix} N+\pi R^2\Delta P \\ T \\ M_x \\ M_y \\ 2\pi R^2\Delta P \end{pmatrix} \qquad (3)$$

where, α is laying angle with respect to z−axis.

(4) Total stiffness equation

The stiffness equation of all layers includes the stiffness matrix of each layer. The axial tension, torsion, and bending stiffness can be

written as a linear sum of the corresponding stiffness of each layer. However, radial stiffness cannot be because each layer has different radial deformation and pressures. The stiffness equation of the whole layer is as follows. The number of layers is 1 for the innermost layer, carcass and 8 for the outer fabric tape.

$$\begin{bmatrix} K_{11} & K_{12} & 0 & 0 & K_{15} & K_{16} & K_{17} & K_{18} & K_{19} & K_{1\,10} & K_{1\,11} & K_{1\,12} \\ K_{21} & K_{22} & 0 & 0 & 0 & 0 & 0 & 0 & K_{2\,9} & 0 & K_{2\,11} & 0 \\ 0 & 0 & K_{33} & 0 & 0 & 0 & 0 & 0 & 0 & 0 & 0 & 0 \\ 0 & 0 & 0 & K_{44} & 0 & 0 & 0 & 0 & 0 & 0 & 0 & 0 \\ K_{51} & 0 & 0 & 0 & K_{55} & 0 & 0 & 0 & 0 & 0 & 0 & 0 \\ K_{61} & 0 & 0 & 0 & 0 & K_{66} & 0 & 0 & 0 & 0 & 0 & 0 \\ K_{71} & 0 & 0 & 0 & 0 & 0 & K_{77} & 0 & 0 & 0 & 0 & 0 \\ K_{81} & 0 & 0 & 0 & 0 & 0 & 0 & K_{88} & 0 & 0 & 0 & 0 \\ K_{91} & K_{9\,2} & 0 & 0 & 0 & 0 & 0 & 0 & K_{99} & 0 & 0 & 0 \\ K_{10\,1} & 0 & 0 & 0 & 0 & 0 & 0 & 0 & 0 & K_{10\,10} & 0 & 0 \\ K_{11\,1} & K_{11\,2} & 0 & 0 & 0 & 0 & 0 & 0 & 0 & 0 & K_{11\,11} & 0 \\ K_{12\,1} & 0 & 0 & 0 & 0 & 0 & 0 & 0 & 0 & 0 & 0 & K_{12\,12} \end{bmatrix} \begin{bmatrix} \frac{\Delta u_z}{L} \\ \frac{\Delta \varphi}{L} \\ \frac{\Delta \Psi_x}{L} \\ \frac{\Delta \Psi_y}{L} \\ \frac{\Delta u_{r.1}}{R_1} \\ \frac{\Delta u_{r.2}}{R_2} \\ \frac{\Delta u_{r.3}}{R_3} \\ \frac{\Delta u_{r.4}}{R_4} \\ \frac{\Delta u_{r.5}}{R_5} \\ \frac{\Delta u_{r.6}}{R_6} \\ \frac{\Delta u_{r.7}}{R_7} \\ \frac{\Delta u_{r.8}}{R_8} \end{bmatrix} = \begin{bmatrix} F_T \\ T_T \\ M_{xT} \\ M_{yT} \\ 2\pi R_1^2 \Delta P_1 \\ 2\pi R_2^2 \Delta P_2 \\ 2\pi R_3^2 \Delta P_3 \\ 2\pi R_4^2 \Delta P_4 \\ 2\pi R_5^2 \Delta P_5 \\ 2\pi R_6^2 \Delta P_6 \\ 2\pi R_7^2 \Delta P_7 \\ 2\pi R_8^2 \Delta P_8 \end{bmatrix} \quad (4)$$

$$K_{11} = \sum_{ISO} \frac{E_i A_i}{1-\nu_i^2} + \sum_{Orthо} E_i A_i + \sum_{Helical} n_i E_i A_i \cos^3 \alpha_i$$

$$K_{12} = K_{21} = \sum_{Helical} n_i E_i A_i R_i \cos^2 \alpha_i \sin \alpha_i$$

$$K_{22} = \sum_{ISO} \frac{E_i I_{z_i}}{2(1+\nu_i)} + \sum_{Orthо} G_i I_{z_i} + \sum_{Helical} n_i E_i A_i R_i^2 \sin^2 \alpha_i \cos \alpha_i$$

$$K_{33} = \sum_{ISO} \frac{E_i I_{x_i}}{1-\nu_i^2} + \sum_{Orthо} E_i I_{x_i} + \sum_{Helical} \frac{1}{2} n_i E_i A_i R_i^2 \cos^3 \alpha_i$$

$$K_{44} = \sum_{ISO} \frac{E_i I_{y_i}}{1-\nu_i^2} + \sum_{Ortho} E_i I_{y_i} + \sum_{Helical} \frac{1}{2} n_i E_i A_i R_i^2 \cos^3 \alpha_i$$

$$K_{55} = E_1 A_1,\ K_{15} = K_{51} = 0,\ K_{66} = \frac{E_2 A_2}{1-\nu_2^2},\ K_{16} = K_{61} = \frac{\nu_2 E_2 A_2}{1-\nu_2^2}$$

$$K_{77} = E_3 A_3,\ K_{17} = K_{71} = 0,\ K_{88} = \frac{E_4 A_4}{1-\nu_4^2},\ K_{18} = K_{81} = \frac{\nu_4 E_4 A_4}{1-\nu_4^2}$$

$$K_{99} = n_5 E_5 A_5 \sin^3 \alpha_5 \tan \alpha_5,\ K_{19} = K_{91} = n_5 E_5 A_5 \sin^2 \alpha_5 \cos \alpha_5$$

$$K_{29} = K_{92} = n_5 E_5 A_5 R_5 \sin^3 \alpha_5$$

$$K_{10\ 10} = \frac{E_6 A_6}{1-\nu_6^2},\ K_{1\ 10} = K_{10\ 1} = \frac{\nu_6 E_6 A_6}{1-\nu_6^2}$$

$$K_{11\ 11} = n_7 E_7 A_7 \sin^3 \alpha_7 \tan \alpha_7,\ K_{1\ 11} = K_{11\ 1} = n_7 E_7 A_7 \sin^2 \alpha_7 \cos \alpha_7$$

$$K_{2\ 11} = K_{11\ 2} = n_7 E_7 A_7 R_7 \sin^3 \alpha_7$$

$$K_{12\ 12} = \frac{E_8 A_8}{1-\nu_8^2},\ K_{1\ 12} = K_{12\ 1} = \frac{\nu_8 E_8 A_8}{1-\nu_8^2}$$

In the above equation, the equations of third and fourth rows are bending stiffness equations, and they are independent of other rows or columns. Therefore, we can write as follows.

$$\begin{bmatrix} K_{11} & K_{12} & K_{15} & K_{16} & K_{17} & K_{18} & K_{19} & K_{1\,10} & K_{1\,11} & K_{1\,12} \\ K_{21} & K_{22} & 0 & 0 & 0 & 0 & K_{2\,9} & 0 & K_{2\,11} & 0 \\ K_{51} & 0 & K_{55} & 0 & 0 & 0 & 0 & 0 & 0 & 0 \\ K_{61} & 0 & 0 & K_{66} & 0 & 0 & 0 & 0 & 0 & 0 \\ K_{71} & 0 & 0 & 0 & K_{77} & 0 & 0 & 0 & 0 & 0 \\ K_{81} & 0 & 0 & 0 & 0 & K_{88} & 0 & 0 & 0 & 0 \\ K_{91} & K_{9\,2} & 0 & 0 & 0 & 0 & K_{99} & 0 & 0 & 0 \\ K_{10\,1} & 0 & 0 & 0 & 0 & 0 & 0 & K_{10\,10} & 0 & 0 \\ K_{11\,1} & K_{11\,2} & 0 & 0 & 0 & 0 & 0 & 0 & K_{11\,11} & 0 \\ K_{12\,1} & 0 & 0 & 0 & 0 & 0 & 0 & 0 & 0 & K_{12\,12} \end{bmatrix} \begin{bmatrix} \frac{\Delta u_z}{L} \\ \frac{\Delta \varphi}{L} \\ \frac{\Delta u_{r,1}}{R_1} \\ \frac{\Delta u_{r,2}}{R_2} \\ \frac{\Delta u_{r,3}}{R_3} \\ \frac{\Delta u_{r,4}}{R_4} \\ \frac{\Delta u_{r,5}}{R_5} \\ \frac{\Delta u_{r,6}}{R_6} \\ \frac{\Delta u_{r,7}}{R_7} \\ \frac{\Delta u_{r,8}}{R_8} \end{bmatrix} = \begin{bmatrix} F_T \\ T_T \\ 2\pi R_1^2 \Delta P_1 \\ 2\pi R_2^2 \Delta P_2 \\ 2\pi R_3^2 \Delta P_3 \\ 2\pi R_4^2 \Delta P_4 \\ 2\pi R_5^2 \Delta P_5 \\ 2\pi R_6^2 \Delta P_6 \\ 2\pi R_7^2 \Delta P_7 \\ 2\pi R_8^2 \Delta P_8 \end{bmatrix} \quad (5)$$

By subtracting the bending stiffness equations, the reduced matrix is 10 x 10. Then the total number of variables is 20, including the eight radial displacements and eight pressure terms. However, since displacements (Δu_z,$\Delta \varphi$) or loads (F_T,T_T) are input, the total number of variables is 18. Moreover, the reduced construction equations provide 10 equations, so an additional 8 equations are needed. These equations are derived from pressure equilibrium and radial continuity conditions.

(5) Pressure equilibrium / radial continuity conditions

In general, the axial tension and bending moment on the flexible riser do not cause a gap between the layers. Under the no-gap condition, the pressure equilibrium conditions and the radial continuity conditions must be satisfied between the layers.

First, carcass does not have pressure difference because the inner

fluid passes through the inside and the outside of the carcass. That is, the following is satisfied.

$$\Delta P_1 = 0 \qquad (6)$$

Next, the following equilibrium condition must be satisfied between adjacent layers.

$$\Delta P_i^{out} = \Delta P_{i+1}^{in},\ i = 1 \text{ to } 7 \qquad (7)$$

In addition, the following relation holds between the inside and outside pressures in the layer reference.

$$\Delta P_i = P_i{}^{out} - P_i{}^{in},\ i = 1 \text{ to } 8 \qquad (8)$$

The above two formulas can be summarized as follows. That is, the sum of the pressure differences of all layers is equal to the difference of the total pressure applied to the model.

$$\sum_{i=1}^{8} \Delta P_i = P_{in} - P_{out} \qquad (9)$$

On the other hand, the following continuous conditions must be satisfied between adjacent layers.

$$\Delta r_i^{out} = \Delta r_{i+1}^{in},\ i = 1 \text{ to } 7 \qquad (10)$$

Moreover, the following relationship holds for the radial deformations of metal layers because their thickness does not change.

$$\Delta r_3^{in} = \Delta r_3^{out},\ \Delta r_5^{in} = \Delta r_5^{out},\ \Delta r_7^{in} = \Delta r_7^{out} \qquad (11)$$

Therefore, the following equations can be summarized.

$$\Delta r_1^{out} = \Delta r_2^{in},\ \Delta r_2^{out} = \Delta r_3^{in} = \Delta r_3^{out} = \Delta r_4^{in},$$

$$\Delta r_4^{out} = \Delta r_5^{in} = \Delta r_5^{out} = \Delta r_6^{in},\ \Delta r_6^{out} = \Delta r_7^{in} = \Delta r_7^{out} = \Delta r_8^{in} \quad (12)$$

On the other hand, the following relation holds between radii and radial displacements. Fig. 13 shows this relationship between radii and radial displacements.

$$R_i + u_{r.i} = \frac{R_i^{in} + \Delta r_i^{in} + R_i^{out} + \Delta r_i^{out}}{2},\ u_{r.i} = \frac{\Delta r_i^{in} + \Delta r_i^{out}}{2} \quad (13)$$

If the above equations are substituted by radial displacements, the following equation can be written.

$$u_{r.1} = \Delta r_2^{in},\ \Delta r_2^{out} = u_{r.3} = \Delta r_4^{in},\ \Delta r_4^{out} = u_{r.5} = \Delta r_6^{in},\ \Delta r_6^{out} = u_{r.7} = \Delta r_8^{in}$$

(14)

If these equations are expressed with respect of $u_{r.i}$:

$$u_{r.2} = \frac{u_{r.1} + u_{r.3}}{2},\ u_{r.4} = \frac{u_{r.3} + u_{r.5}}{2},\ u_{r.6} = \frac{u_{r.5} + u_{r.7}}{2} \quad (15)$$

On the other hand, the change in thickness of the polymer layer can be expressed by the following equation.

$$\Delta t_i = \Delta P_i \frac{(2-\nu_i){R_i}^2}{2E_i t_i} - \frac{\nu_i N_i R_i}{A_i E_i},\ i = 2, 4, 6, 8 \quad (16)$$

Therefore, it can be summarized as follows.

$$u_{r.3} - u_{r.1} = \Delta t_2,\ u_{r.5} - u_{r.3} = \Delta t_4,\ u_{r.7} - u_{r.5} = \Delta t_6 \quad (17)$$

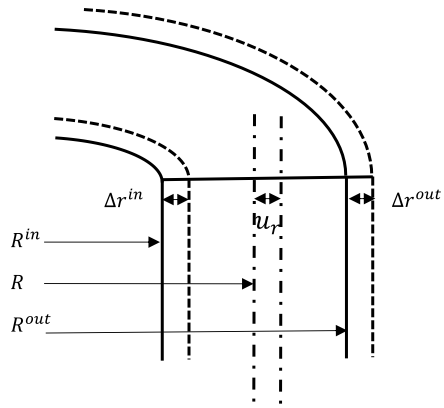

Fig. 13 The concept of radial deformation

Additional equations which are bold (6, 9, 15, 17) come from the pressure equilibrium condition and the continuous condition of the radial displacement.

If the condition of (6) is substituted in (5), $\mathbf{\Delta u_{r.1} = 0}$ can be obtained. Then (5) can be expressed as:

$$[A_{stiff}][A_{reviprocal}]\begin{bmatrix}\frac{\Delta u_z}{L}\\ \frac{\Delta\varphi}{L}\\ \Delta u_{r.1}\\ \Delta u_{r.2}\\ \Delta u_{r.3}\\ \Delta u_{r.4}\\ \Delta u_{r.5}\\ \Delta u_{r.6}\\ \Delta u_{r.7}\\ \Delta u_{r.8}\end{bmatrix} = [A_{square}]\begin{bmatrix}F_T\\ T_T\\ \Delta P_1\\ \Delta P_2\\ \Delta P_3\\ \Delta P_4\\ \Delta P_5\\ \Delta P_6\\ \Delta P_7\\ \Delta P_8\end{bmatrix} \qquad (18-a)$$

where

$$\begin{bmatrix} K_{11} & K_{12} & K_{16} & K_{17} & K_{18} & K_{19} & K_{1\,10} & K_{1\,11} & K_{1\,12}\\ K_{21} & K_{22} & 0 & 0 & 0 & K_{2\,9} & 0 & K_{2\,11} & 0\\ K_{61} & 0 & K_{66} & 0 & 0 & 0 & 0 & 0 & 0\\ K_{71} & 0 & 0 & K_{77} & 0 & 0 & 0 & 0 & 0\\ K_{81} & 0 & 0 & 0 & K_{88} & 0 & 0 & 0 & 0\\ K_{91} & K_{9\,2} & 0 & 0 & 0 & K_{99} & 0 & 0 & 0\\ K_{10\,1} & 0 & 0 & 0 & 0 & 0 & K_{10\,10} & 0 & 0\\ K_{11\,1} & K_{11\,2} & 0 & 0 & 0 & 0 & 0 & K_{11\,11} & 0\\ K_{12\,1} & 0 & 0 & 0 & 0 & 0 & 0 & 0 & K_{12\,12}\end{bmatrix} = [A_{stiff}]$$

$$\begin{bmatrix} 1 & 0 & 0 & 0 & 0 & 0 & 0 & 0 & 0 \\ 0 & 1 & 0 & 0 & 0 & 0 & 0 & 0 & 0 \\ 0 & 0 & 1/R_2 & 0 & 0 & 0 & 0 & 0 & 0 \\ 0 & 0 & 0 & 1/R_3 & 0 & 0 & 0 & 0 & 0 \\ 0 & 0 & 0 & 0 & 1/R_4 & 0 & 0 & 0 & 0 \\ 0 & 0 & 0 & 0 & 0 & 1/R_6 & 0 & 0 & 0 \\ 0 & 0 & 0 & 0 & 0 & 0 & 1/R_6 & 0 & 0 \\ 0 & 0 & 0 & 0 & 0 & 0 & 0 & 1/R_7 & 0 \\ 0 & 0 & 0 & 0 & 0 & 0 & 0 & 0 & 1/R_8 \end{bmatrix} = [A_{reviprocal}]$$

$$\begin{bmatrix} 1 & 0 & 0 & 0 & 0 & 0 & 0 & 0 & 0 \\ 0 & 1 & 0 & 0 & 0 & 0 & 0 & 0 & 0 \\ 0 & 0 & 2\pi R_2^2 & 0 & 0 & 0 & 0 & 0 & 0 \\ 0 & 0 & 0 & 2\pi R_3^2 & 0 & 0 & 0 & 0 & 0 \\ 0 & 0 & 0 & 0 & 2\pi R_4^2 & 0 & 0 & 0 & 0 \\ 0 & 0 & 0 & 0 & 0 & 2\pi R_5^2 & 0 & 0 & 0 \\ 0 & 0 & 0 & 0 & 0 & 0 & 2\pi R_6^2 & 0 & 0 \\ 0 & 0 & 0 & 0 & 0 & 0 & 0 & 2\pi R_7^2 & 0 \\ 0 & 0 & 0 & 0 & 0 & 0 & 0 & 0 & 2\pi R_8^2 \end{bmatrix} = [A_{square}]$$

$$[A_{square}]^{-1}[A_{stiff}][A_{reviprocal}] \begin{bmatrix} \frac{\Delta u_z}{L} \\ \frac{\Delta \varphi}{L} \\ \Delta u_{r.1} \\ \Delta u_{r.2} \\ \Delta u_{r.3} \\ \Delta u_{r.4} \\ \Delta u_{r.5} \\ \Delta u_{r.6} \\ \Delta u_{r.7} \\ \Delta u_{r.8} \end{bmatrix} = [A] \begin{bmatrix} \frac{\Delta u_z}{L} \\ \frac{\Delta \varphi}{L} \\ \Delta u_{r.1} \\ \Delta u_{r.2} \\ \Delta u_{r.3} \\ \Delta u_{r.4} \\ \Delta u_{r.5} \\ \Delta u_{r.6} \\ \Delta u_{r.7} \\ \Delta u_{r.8} \end{bmatrix} = \begin{bmatrix} F_T \\ T_T \\ \Delta P_1 \\ \Delta P_2 \\ \Delta P_3 \\ \Delta P_4 \\ \Delta P_5 \\ \Delta P_6 \\ \Delta P_7 \\ \Delta P_8 \end{bmatrix} \qquad (18-\text{b})$$

Next, (16) and (17) can be written as following where radial deformation of inner radius of second layer is Δr_2^{in}.

$$\Delta u_{r.2} = \Delta r_2^{in} + \frac{\Delta t_2}{2}$$

$$= \Delta r_2^{in} + \frac{{R_2}^2}{t_2}\frac{2-\nu_2}{4E_2}\Delta P_2 - \frac{\nu_2 R_2}{2A_2E_2}\left(\frac{A_2E_2}{1-\nu_2^2}\frac{\Delta u_z}{L} + \frac{\nu_2 A_2 E_2}{1-\nu_2^2}\frac{\Delta u_{r.2}}{R_2} - \pi^2 R_2^2 \Delta P_2\right)$$

In summary, above equation can be written as:

$$-\Delta r_2^{in} + \left(1 + \frac{\nu_2^2}{2(1-\nu_2^2)}\right)\Delta u_{r.2} + \frac{\nu_2 R_2}{2(1-\nu_2^2)}\frac{\Delta u_z}{L} - \left(\frac{{R_2}^2}{t_2}\frac{2-\nu_2}{4E_2} + \frac{\nu_2 \pi^2 R_2^3}{2A_2E_2}\right)\Delta P_2 = 0$$

$$-\Delta r_2^{in} + \alpha_2 \Delta u_{r.2} + \beta_2 \frac{\Delta u_z}{L} - \gamma_2 \Delta P_2 \quad (19)$$

where $\alpha_2 = \left(1 + \frac{\nu_2^2}{2(1-\nu_2^2)}\right), \beta_2 = \frac{\nu_2 R_2}{2(1-\nu_2^2)}, \gamma_2 = \left(\frac{{R_2}^2}{t_2}\frac{2-\nu_2}{4E_2} + \frac{\nu_2 \pi^2 R_2^3}{2A_2 E_2}\right)$

Likewise,

$$-\Delta u_{r.3} + \alpha_4 \Delta u_{r.4} + \beta_4 \frac{\Delta u_z}{L} - \gamma_4 \Delta P_4 \quad (20)$$

$$-\Delta u_{r.5} + \alpha_6 \Delta u_{r.6} + \beta_6 \frac{\Delta u_z}{L} - \gamma_6 \Delta P_6 \quad (21)$$

$$-\Delta u_{r.7} + \alpha_8 \Delta u_{r.8} + \beta_8 \frac{\Delta u_z}{L} - \gamma_8 \Delta P_8 \quad (22)$$

Then (9), (15), (18−b), (19−22) can be combined as (23).

$$\begin{bmatrix} A & B \\ C & D \end{bmatrix} \begin{vmatrix} \frac{\Delta u_z}{L} \\ \frac{\Delta \varphi}{L} \\ \Delta u_{r.1} \\ \Delta u_{r.2} \\ \Delta u_{r.3} \\ \Delta u_{r.4} \\ \Delta u_{r.5} \\ \Delta u_{r.6} \\ \Delta u_{r.7} \\ \Delta u_{r.8} \\ \Delta P_2 \\ \Delta P_3 \\ \Delta P_4 \\ \Delta P_5 \\ \Delta P_6 \\ \Delta P_7 \\ \Delta P_8 \\ \Delta P_{total} \end{vmatrix} = \begin{vmatrix} F_T \\ T_T \\ 0 \\ 0 \\ 0 \\ 0 \\ 0 \\ 0 \\ 0 \\ 0 \\ 0 \\ 0 \\ 0 \\ 0 \\ 0 \\ 0 \\ 0 \\ 0 \end{vmatrix} \quad (23)$$

$$\begin{bmatrix} 0 & 0 & 0 & 0 & 0 & 0 & 0 & 0 \\ 0 & 0 & 0 & 0 & 0 & 0 & 0 & 0 \\ -1 & 0 & 0 & 0 & 0 & 0 & 0 & 0 \\ 0 & -1 & 0 & 0 & 0 & 0 & 0 & 0 \\ 0 & 0 & -1 & 0 & 0 & 0 & 0 & 0 \\ 0 & 0 & 0 & -1 & 0 & 0 & 0 & 0 \\ 0 & 0 & 0 & 0 & -1 & 0 & 0 & 0 \\ 0 & 0 & 0 & 0 & 0 & -1 & 0 & 0 \\ 0 & 0 & 0 & 0 & 0 & 0 & -1 & 0 \end{bmatrix} = [B],$$

$$\begin{bmatrix} \beta_2 & 0 & \alpha_2 & 0 & 0 & 0 & 0 & 0 & 0 \\ 0 & 0 & -2 & 1 & 0 & 0 & 0 & 0 & 0 \\ \beta_4 & 0 & 0 & -1 & \alpha_4 & 0 & 0 & 0 & 0 \\ 0 & 0 & 0 & 1 & -2 & 1 & 0 & 0 & 0 \\ \beta_6 & 0 & 0 & 0 & 0 & -1 & \alpha_6 & 0 & 0 \\ 0 & 0 & 0 & 0 & 0 & 1 & -2 & 1 & 0 \\ \beta_8 & 0 & 0 & 0 & 0 & 0 & 0 & -1 & \alpha_8 \\ 0 & 0 & 0 & 0 & 0 & 0 & 0 & 0 & 0 \end{bmatrix} = [C],$$

$$\begin{bmatrix} -\gamma_2 & 0 & 0 & 0 & 0 & 0 & 0 & 0 \\ 0 & 0 & 0 & 0 & 0 & 0 & 0 & 0 \\ 0 & 0 & 0 & -\gamma_4 & 0 & 0 & 0 & 0 \\ 0 & 0 & 0 & 1 & 0 & 0 & 0 & 0 \\ 0 & 0 & 0 & 0 & 0 & -\gamma_6 & 0 & 0 \\ 0 & 0 & 0 & 0 & 0 & 1 & 0 & 0 \\ 0 & 0 & 0 & 0 & 0 & 0 & 0 & -\gamma_8 \\ 1 & 1 & 1 & 1 & 1 & 1 & 1 & 0 \end{bmatrix} = [D]$$

Finally, using direct method, all variables can be solved.

2.1.2. Behavior about bending moment

On the other hand, when the constitutive equation for the entire model is obtained, it can be confirmed that the bending moment acts independently of the axisymmetric load.

$$M_{xT} = K_{33}\frac{\Delta\Psi_x}{L},\ M_{yT} = K_{44}\frac{\Delta\Psi_y}{L} \qquad (24)$$

$$K_{33} = \sum_{ISO}\frac{E_i I_{x_i}}{(1-\nu_i)^2} + \sum_{Orthо} E_i I_{x_i} + \sum_{Helical} Bending\ \ stiffness \quad (25)$$

$$K_{44} = \sum_{ISO}\frac{E_i I_{y_i}}{(1-\nu_i)^2} + \sum_{Orthо} E_i I_{y_i} + \sum_{Helical} Bending\ \ stiffness \quad (26)$$

Here, the bending stiffness of the tensile armor is determined by the slip/stick condition. According to Kraincanic et. al (2001), partial slippage occurs when the curvature exceeds the minimum critical curvature, and all tendons get to slip when the curvature reach its maximum critical curvature.

(1) No slip condition $K \leq K_{cr,min}$

$$EI_0 = \frac{1}{2} nEAR^2 \cos^3 \alpha \quad (27)$$

(2) During the process of becoming a slip $K_{cr,min} < K \leq \frac{\pi}{2} K_{cr,min}$

$$EI = EI_0 - \frac{2}{\pi} EI_0 \left[\xi \arccos \frac{K_{cr}^{min}}{K} - \frac{1}{2} \sin \left(2\xi \arccos \frac{K_{cr}^{min}}{K} \right) \right] \quad (28)$$

(3) Full slip range $K > \frac{\pi}{2} K_{cr,min}$

$$EI = 0 \quad (29)$$

Here you can write: $K_{cr,min} = \frac{k_{out}^{fr} P_{out} + k_{in}^{fr} P_{in}}{Et \cos^2 \alpha \sin \alpha}$

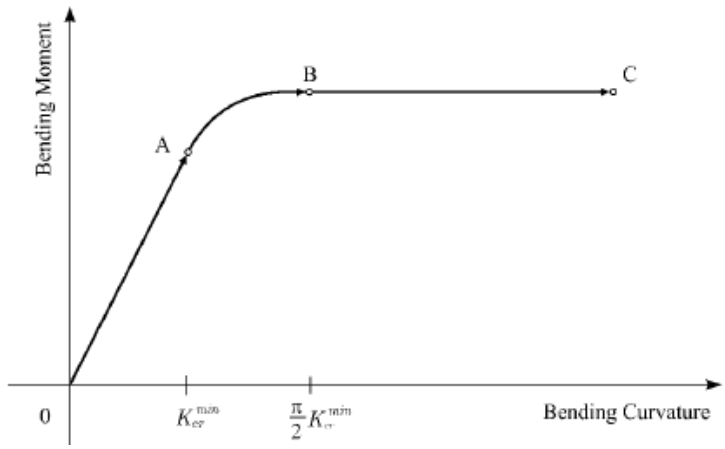

Fig. 14 Schematic bending moment−curvature relationship of a flexible riser helical layer, Kraincanic et. al (2001)

Therefore, the critical curvature is determined when the contact pressure between the layers is determined with respect to the axisymmetric load, and the nonlinear bending stiffness is determined thereby.

2.2. Analytical Explanation of Radial Buckling

In the flood annulus state, the tape layer is located outside and delays the radial expansion of the tensile armor. Then the expansion of the tendons applies contact pressure to the tape, and this can increase the stress of tape layer. Saevik (2012) explains that the stress of tape is related to the axial stress of the tendon.

$$\sigma_{tape} = \frac{R_{tape}}{t_{tape}} p_t = \frac{R_{tape}}{t_{tape}} \frac{T_w tan^2\alpha}{2\pi R_{T.A.}^2} = \frac{R_{tape}}{t_{tape}} \frac{nA\sigma_a cos\alpha tan^2\alpha}{2\pi R_{T.A.}^2} \quad (30)$$

Therefore, if the stress on the tape exceeds the yield strength, the tape can no longer support the expansion of the tendon, and the displacement becomes large rapidly. Therefore, axial stress on the tendon causing radial buckling can be obtained.

3. Research Model

3.1. Properties of 2.5-inch Flexible Riser

The model of Witz (1996) is very useful. This is because most of the geometric information and material properties and the results of axial/bending stiffness test are provided. The Table 2 shows the geometry information and material properties of the 2.5-inch flexible riser.

Table 2 Material properties and geometric information of the model

No.	Layer	ID (mm)	Material	t (mm)	E (GPa)	ν	# of strips	Sectional area (mm^2)	α (deg.)	Yield strength (MPa)	Tensile strength (MPa)	Tensile strain (%)
1	Carcass	63.2	AISI 304*	3.5	193	0.3	1	19.6	−87.5	215	505	40.0
2	Pressure sheath	70.2	Nylon 12	4.9	0.284	0.29	1	−	−	30	36	
3	Pressure armor	80.0	Steel AFNOR FI 15	6.2	205	0.3	2	51.5	−85.5	780	900	1.0
4	Anti-friction layer	92.5	Rilsan Nylon 11	1.5	0.301/0.150	0.29	1	−	−84.2	20**	25**	3.0**
5	Inner tensile armor layer	95.5	Steel AFNOR FI 41	3	205	0.3	40	18	−35	1100	1400	1.0
6	Anti-friction Layer	101.5	Rilsan Nylon 11	1.5	0.301/0.150	0.29	1	−	−84.7	20	25	3.0
7	Outer tensile armor layer	104.5	Steel AFNOR FI 41	3	205	0.3	44	18	35	1100	1400	1.0
8−1	Fabric tape	110.5	Type PVC	0.5	0.6/0.3***	0.29	1	−	−84	−	−	−
8−2	Outer sheath	110.5	PA11****	0.5	0.6	0.29	1	−	−	30	36	22.0

* http://www.matweb.com

** They are assumed since there are no published values.

*** Axial stiffness = 600 MPa, transverse stiffness= 300 MPa

**** Refer to the brochure of Rilsan PA11 from ATOFINA Chemicals, Inc.

For the nonlinear ultimate strength analysis, the values of yield strength and tensile strength of all materials were used. Most of the values were from Witz (1996), but some information comes from other sources. For example, the properties of AFNOR 15 and 41 were from Sousa (2005), and yield strength and tensile strength of the fabric tape were used the values of PA11, which is usually used as the outer sheath material.

On the other hand, tape layers must be orthotropic layer because their axial and transverse stiffness are different. However, orthotropic modeling of a tape layer with very small elastic moduli compared to metal layers has a problem of poor convergence of the analysis. Therefore, in this research, tape layers are assumed isotropic. The Fig. 15 represents the concept of isotropic assumption. The bigger stiffness (transverse direction) is adopted for the elastic modulus of isotropic layer. Moreover, the validity of the above assumptions is verified through the results of elastic analysis.

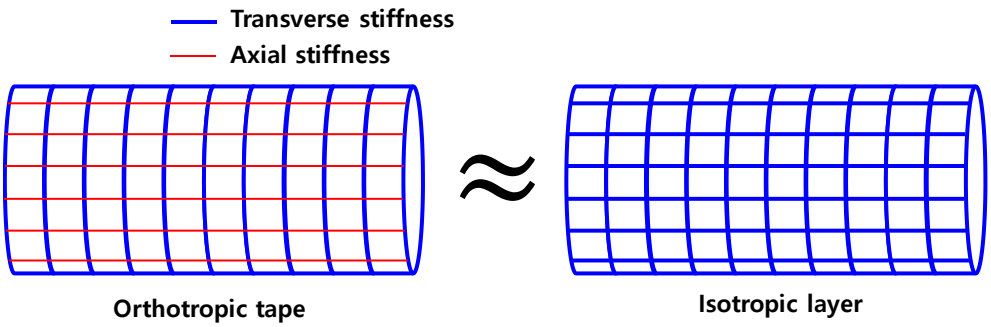

Fig. 15 Isotropic assumption used in this research

3.2. Simplification of Geometry of Layers

Next simplification in this study is a complex cross-sectional shape. In particular, the cross-sectional shapes of the carcass and pressure armor are very complex, so those layers involve not only contact with other layers, but also a self-contact called 'interlocking'. Therefore, it is difficult to perform technically stable nonlinear analysis with a model reflecting all the shapes of the layers above.

Sousa et. al (2005) proposed replacing layers such as carcass and pressure armor with equivalent layers, and this method was used in this study. The following equations show how to obtain equivalent layer thickness, elastic modulus, and shear modulus.

$$t_{\mathrm{eq.}} = \sqrt{12\frac{I_{eq}}{A}},\ E_{\mathrm{eq.}} = \left(\frac{A \cdot n}{L_P \cdot t_{eq.}}\right) E,\ G_{\mathrm{eq.}} = \left(3\ \frac{J \cdot n}{L_P \cdot {t_{eq.}}^3}\right) G,$$

$$I_{eq} = 12 \cdot n_t \cdot \frac{I_y^2}{L_t} \cdot \frac{1-\nu^2}{h^3} \qquad (31)$$

where, $t_{\mathrm{eq.}}$ is equivalent thickness, A is the area and I_{y} is the smaller second moment about central axis of cross-section. $E_{\mathrm{eq.}}$ is the equivalent elastic modulus, n is the number of wires, E is the elastic modulus of material, $G_{\mathrm{eq.}}$is the equivalent shear modulus, J is the polar moment of cross-sectional area, G is the shear modulus of material, L_P is the pitch length of the tendon. The Fig. 16 shows the layers before and after simplification of geometry. The direction of $E_{\mathrm{eq.}}$ is tilted as α from axial axis. Therefore, $E_{\mathrm{eq.}}$ can be divided into two directions, E_1 and E_2 which are axial and circumferential elastic modulus.

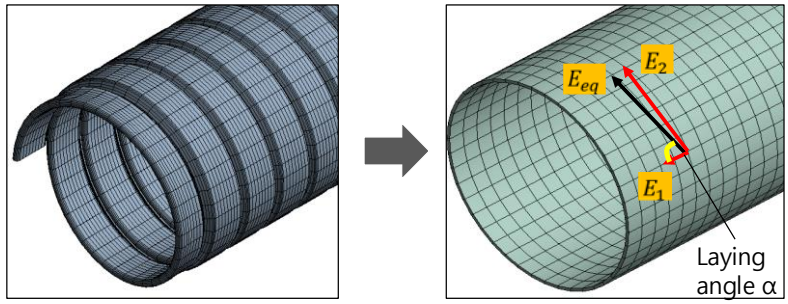

Fig. 16 Simplification of geometry

Using an equivalent orthotropic layer can simplify the FE model and solve the convergence problem that occurs in nonlinear FE analysis. However, the method proposed by Sousa (2005) is valid only to the extent that interlocking of carcass and pressure armor does not occur. The above layers have very low axial stiffness within a certain range. However, after interlocking, axial stiffness increases rapidly.

Sectional shapes are used to determine the maximum strain when interlocking occurs for the carcass and pressure armor. These two layers consist of a periodic repetition of cross-sectional shapes and the interlocking occurs subjected to a certain amount of tension or contraction. The range of tensile strain without interlocking is between −5.6% and 4.5% for carcass and between −6.7% and 6.7% for pressure armor. These strain rage is the condition for the method of Sousa (2005). In this research, all numerical analyses are controlled to be within this range. Fig. 17 shows the cross-section of carcass and pressure armor. Fig. 18 shows the interlocking phenomena of carcass and pressure armor for elongation and shortening.

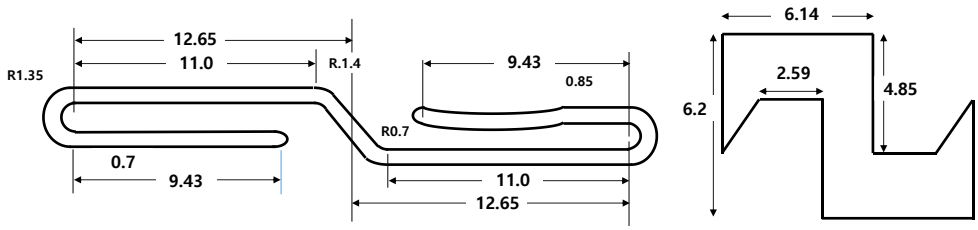

Fig. 17 Cross-section of carcass (L) and pressure armor(R)

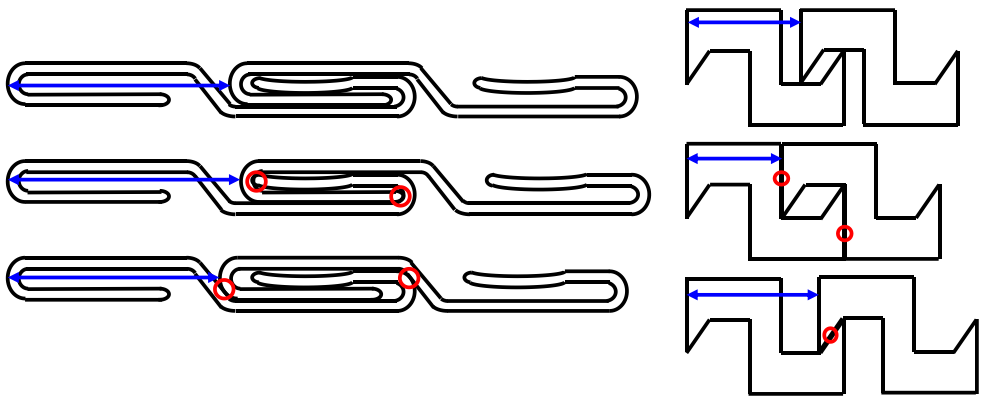

Fig. 18 Interlocking due to elongation and shortening carcass (L), pressure armor (R)

4. Numerical Method

4.1. Process of Numerical Method

4.1.1.Mesh Generation

The numerical method proceeds in the following order.

- Input the material properties and geometric information
- Generate a mesh

- Set contact conditions and analysis conditions
- Check the desired results.

2-noded beam, 4-noded shell, and 8-noded solid are used to construct the FE model. A linear function is used as an interpolation function. In the previous section, through the simplification of geometry, carcass and pressure armor are replaced with equivalent layers. Since these metal layers are rigid in the radial direction, that is, their thickness change can be ignored. Moreover, thickness is very thinner than radius. Therefore, it is appropriate to model with shell elements. On the other hand, since the tensile armor layers have very small cross sections and slender shapes, they are modeled with beam elements. The remaining sheath and tape layers have small stiffness compared to metal layers, so thickness changes cannot be ignored. Therefore, solid elements seem to be suitable. However, the shell elements are more suitable than the solid elements because the thickness is very thin compared to the radius. Therefore, in this study, shell model and solid model are constructed respectively according to the elements of polymer layers. Table 3 lists properties of elements and materials of FE model.

Table 3 Properties of elements and materials of FE model

	Layer	Type of Material	Model	Type of Element (Model 1. SHELL)	Type of Element (Model 2. SOLID)
1	Carcass	Orthotropic	Cylinder	SHELL181	
2	Pressure sheath	Isotropic		SHELL181	SOLID185
3	Pressure armor	Orthotropic		SHELL181	
4	Anti-friction tape	Isotropic	Helical tendons	SHELL181	SOLID185
5	Inner tensile armor layer	Isotropic	Cylinder	BEAM188	
6	Anti-friction tape	Isotropic	Helical tendons	SHELL181	SOLID185
7	Outer tensile armor layer	Isotropic	Cylinder	BEAM188	
8	Fabric tape	Isotropic		SHELL181	SOLID185

4.1.2. Contact Setting

Next, contact conditions are set. The contact type is a friction type. This means that it is possible to contact and separate in the

vertical direction and to slip in the horizontal direction when a force exceeding the frictional force is applied. The coefficient of friction between elements is 0.1 as shown in Saevik (1995). Moreover, a pure penalty method is used for contact algorithm. Under real conditions, any penetration is not allowed into an inward layer, but a slight penetration is inevitable with the contact algorithm. This method can be used for various contact problems and has an advantage of being more convergent than other methods. The following equation shows the concept of the pure penalty method.

$$F_n = k_n x_p,\ F_t = k_t x_p \qquad (32)$$

ANSYS Mechanical provides the values of stiffness coefficients (FKN, FKT) to allow the user to control the magnitude of contact stiffness. The contact stiffness is automatically calculated for each iteration during the analysis. The new stiffness value is updated by multiplying this value by the user-specified coefficient. If the contact stiffness coefficient is increased, the accuracy of the analysis is improved, but the convergence becomes poor. In general, convergence and accuracy tend to be inversely proportional in nonlinear analysis. Therefore, it is difficult to find the exact solution at a time, and it is necessary to try to find the exact solution within the limit of convergence through several iterations. In the ANSYS

Guidance (R.15.0), the stiffness coefficients are proposed to be 0.01 to 1.0. In this study, 0.1 was used for FKN and 1.0 was used for FKT. CONTA175/TARGE170 elements are used to realize the contact mechanism between helical tendons and cylindrical layers, and CONTA174/TARGE170 are applied between the cylindrical layers. Table 4 shows the information on contact pair's elements and properties.

Table 4 Information on contact pairs' elements and properties

<table>
<tr><th rowspan="2"></th><th rowspan="2">Contact</th><th rowspan="2">Target</th><th rowspan="2">Contact type</th><th rowspan="2">Contact elements</th><th colspan="2">FTOL</th></tr>
<tr><th>SHELL</th><th>SOLID</th></tr>
<tr><td>1</td><td>Pressure sheath</td><td>Carcass</td><td rowspan="7">Frictional ($\mu = 0.1$)</td><td rowspan="3">Conta174/ Target170 (surface – surface)</td><td rowspan="7">Larger than 1%</td><td rowspan="7">1%</td></tr>
<tr><td>2</td><td>Pressure sheath</td><td>Pressure armor</td></tr>
<tr><td>3</td><td>Anti–friction 1</td><td>Pressure armor</td></tr>
<tr><td>4</td><td>Tensile armor 1</td><td>Anti–friction 1</td><td rowspan="4">Conta175/ Target170 (node–surface)</td></tr>
<tr><td>5</td><td>Tensile armor 1</td><td>Anti–friction 2</td></tr>
<tr><td>6</td><td>Tensile armor 2</td><td>Anti–friction 2</td></tr>
<tr><td>7</td><td>Tensile armor 2</td><td>Fabric tape</td></tr>
</table>

On the other hand, ANSYS Mechanical allows the user to determine the maximum penetration tolerance of an element. In

physical phenomena, such a penetration of the material doesn't happen, but in the numerical method, even a very small amount of penetration is inevitable. In ANSYS guidance (R.15), the penetration allowance factor (FTOL) of the element is recommended as 1% of the element thickness. In this study, FTOL was set to 1% when the target body was a solid element. However, when the target body is a shell element, the FTOL should be greater than 1%. The reason is due to the difference between solid and shell elements for contact.

When a solid element makes contact with another element, deformation occurs in the thickness direction. However, the shell element cannot reflect the deformation in thickness direction, thus, the contact mechanism can differ from the actual phenomenon. This can be realized by allowing the penetration tolerance as much as the penetration of neighboring layers. In ANSYS, shell element can have a virtual rigid thickness and it differs from solid element which can deform in thickness direction. Fig. 19 shows the virtual thickness used for shell element in ANSYS mechanical and FTOL to realize the thicknesswise deformation.

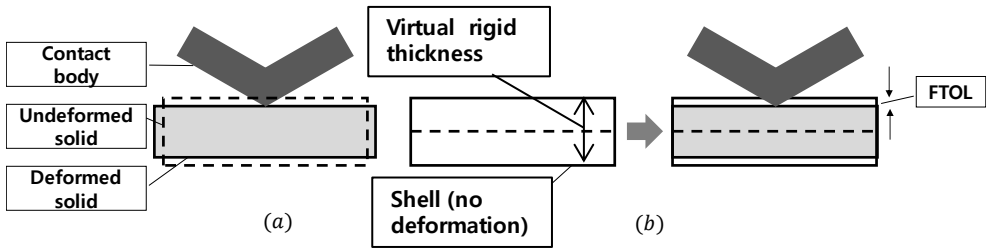

Fig. 19 Difference of (a) solid and (b) shell elements with respect to deformation

CONTA175 / TARGE170 elements are used to realize the contact mechanism between nodes of a tendon layer and surfaces of its neighboring solid layers in the 8-layered solid models (or shell layers in the 8-layered shell model). Similarly, CONTA174 / TARGE170 elements are employed between two adjoining surfaces of shell or solid layers. The same contact elements are used for the 8-layered solid and shell models. The option of 'asymmetric' is used so that the contact body cannot penetrate the target body. More details on this can be found in the elastic analysis section.

4.1.3.Analysis Setting

Next, boundary conditions and various analysis options are set. In the axisymmetric load analysis, load control or displacement control is used. All nodes at both ends rigidly constrain to a remote point located at the center of the plane like Fig. 20. One end is restrained

for all degrees of freedom to prevent the rigid body motion, and a force or forced displacement is applied at the other end. For bending moment analysis, forced displacement (curvature) is applied at both ends. In addition, a rigid link is added at the middle of the model, which serves to match the symmetry of the model and avoid any sudden displacement. The Table 5 represents boundary conditions for axial load and bending moment.

Table 5 Boundary conditions for axial load and bending moment

<table>
<tr><th rowspan="3">DOF</th><th colspan="3">Axial Load</th><th colspan="3">Bending Moment</th></tr>
<tr><th rowspan="2">RP1</th><th colspan="2">RP2</th><th rowspan="2">RP1</th><th rowspan="2">RP2</th><th rowspan="2">RP3</th></tr>
<tr><th>Force control</th><th>Displ. control</th></tr>
<tr><td>X</td><td rowspan="6">Fixed</td><td rowspan="6">Free</td><td rowspan="2">Fixed</td><td rowspan="3">Fixed</td><td rowspan="2">Fixed</td><td rowspan="6">Free</td></tr>
<tr><td>Y</td></tr>
<tr><td>Z</td><td>Control</td><td rowspan="2">Free</td></tr>
<tr><td>RX</td><td rowspan="3">Fixed</td><td colspan="2">Control</td></tr>
<tr><td>RY</td><td rowspan="2">Fixed</td><td rowspan="2">Fixed</td></tr>
<tr><td>RZ</td></tr>
</table>

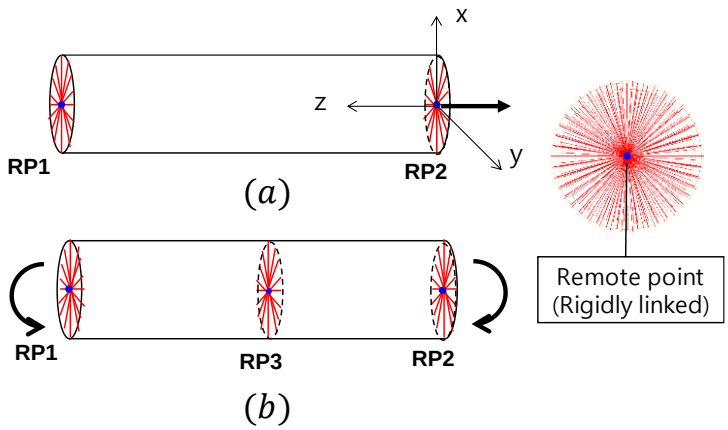

Fig. 20 Remote points for (a) axial load and (b) bending moment

On the other hand, ANSYS performs iterative analysis using the Newton – Raphson method to converge the solution in the nonlinear analysis. When it converges in each section, it automatically goes to the next section. In this study, the number of sub-steps was automatically determined by turning on the auto time stepping option. In addition, the large deflection option was turned on only for the ultimate strength analysis and off for the elastic analysis.

4.2. Simplification of Composition of Model

The model created through the previous series is an 8-layered model. However, the above model is also difficult to perform the ultimate strength analysis because of the complex interaction of multiple layers. Therefore, one additional simplification is proposed.

Failure mode due to axial compressive force causes the tensile armor to swell outwards causing failure of the outer tape. Due to the specificity of the failure mode, failure of the outer tape will cause buckling of the tensile armor layer, and the flexible riser will no longer be able to perform its function.

Depending on whether they have direct effects, 8 layers are divided into two parts: part A and part B. The layers of part A are closely related to radial buckling, and they are fabric tape, outer anti-friction tape, and a pairs of tensile armor layers. On the other hand, the layers of part B are not closely related to radial buckling, and they are carcass, pressure sheath, pressure armor, and inner anti-friction tape. The role of the layers of Part B is mainly to withstand pressure. Therefore, an equivalent pressure layer is proposed to replace these layers. That is, by reducing the number of layers, the problem of convergence is improved. As a result, the number of contact elements decreased by 84% and the total number of elements decreased by 69%. The Fig. 21 represents the concept of simplification of composition of model.

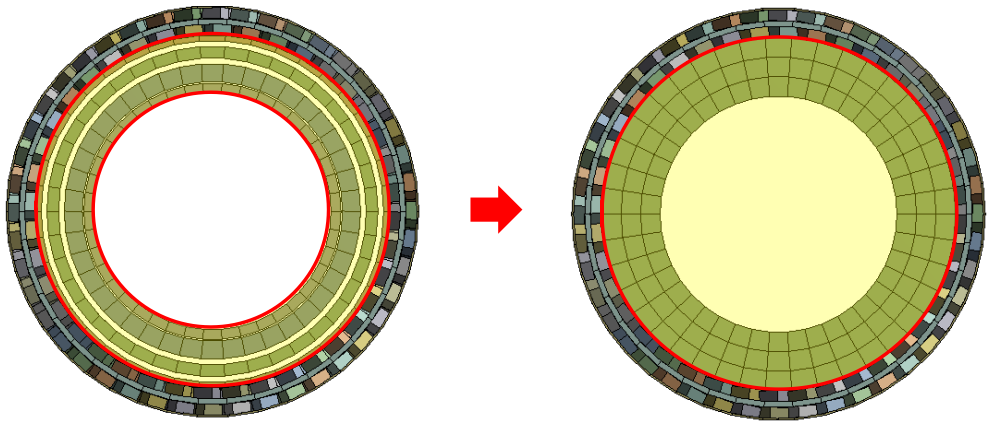

Fig. 21 Simplification of composition of model

The entire equivalent layer is determined to have the same behavior with respect to the layers of part B and the axisymmetric load and bending moment. The geometric information and properties of the EQP are determined according to these criteria. The EQP is designed to replace layers of part B. Part B layers include orthotropic layers carcass and pressure armor layers, so EQP can also be considered an orthotropic layer. The outer radius of the EQP was equal to the inner radius of the inner tensile armor for contact reasons. Therefore, to determine the EQP, the thickness (t^*), axial elastic modulus (E_1^*), radial elastic modulus (E_2^*), and shear modulus (G_{12}^*) must be determined as Fig. 22.

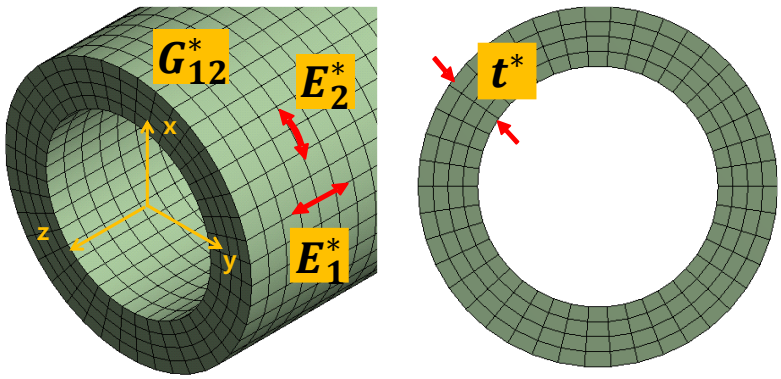

Fig. 22 Variables of equivalent pressure layer

4.2.1. Determination of EQP

The layers of Part B were replaced by one EQP because they do not directly affect the failure modes for axial compressive forces. The outer radius of the EQP is equal to that of inner anti-friction tape (the 4th layer). This is because it is in contact with the inner tensile armor (the 5th layer). In addition, because the carcass and pressure armor are orthotropic layers, EQP also is assumed orthotropic. EQP should have the same behavior within the elastic range for the axially symmetric load and bending moments of the layers of part B. To determine the EQP, the analytical method proposed by Bahtui et. al (2009) is adopted. The equations below show the behavior of various loads on the orthotropic cylinder layer, which are same with equation (2). Each row shows axial tension,

torsion, moment about x−axis, moment about y−axis, and stiffness equation for pressure.

- (2−1) $AE_1^* \frac{\Delta u_z}{L} = N + \pi R^2 \Delta P$ (axial stiffness)
- (2−2) $G_{12}^* I_z \frac{\Delta \varnothing}{L} = T$ (torsional stiffness)
- (2−3) $E_1^* I_x \frac{\Delta \psi_x}{L} = M_x$ (bending stiffness about x−axis)
- (2−4) $E_1^* I_y \frac{\Delta \psi_y}{L} = M_y$ (bending stiffness about y−axis)
- (2−5) $AE_2^* \frac{\Delta u_r}{R} = 2\pi R^2 \Delta P$ (radial stiffness)

The cylindrical layer is axisymmetric, so there is no difference in the behavior under the bending moment about the normal and bi−normal axes in Fig. 12. Thus, the above equation can be reduced to four. Part B's layers and EQP should have the same displacement when given the same load. Therefore, the loads N, ΔP, T, M_x and displacement, $\frac{\Delta u_z}{L}$, $\frac{\Delta \varnothing}{L}$, $\frac{\Delta \psi_x}{L}$, $\frac{\Delta u_r}{R}$ will have the subscript 'pt B' which means these variables are from the Part B. Among the remaining variables, the most frequently included variables are t^*. That is, R, A, I_z, and $I_x(I_y)$ are functions of t^*.

$$\mathrm{R} = \mathrm{R_{AF}} - \mathrm{t^*}/2,\ \mathrm{A} = \pi\left[(\mathrm{R} + \mathrm{t^*}/2)^2 - (\mathrm{R} - \mathrm{t^*}/2)^2\right],$$

$$\mathrm{I_z} = \frac{\pi}{2}\left[(\mathrm{R} + \mathrm{t^*}/2)^4 - (\mathrm{R} - \mathrm{t^*}/2)^4\right],\ \mathrm{I_x} = \mathrm{I_z}/2 \quad (33)$$

Then above stiffness equations are written again as follows.

$$AE_1^*\left(\frac{\Delta u_z}{L}\right)_{Pt\ B} = N_{Pt\ B} + \pi R^2 \Delta P_{Pt\ B} \quad (34)$$

$$E_1^* I_x \left(\frac{\Delta \psi_x}{L}\right)_{Pt\ B} = (M_x)_{Pt\ B} \quad (35)$$

$$AE_2^*\left(\frac{\Delta u_r}{R}\right)_{Pt\ B} = 2\pi R^2 \Delta P_{Pt\ B} \quad (36)$$

$$G_{12}^* I_z \left(\frac{\Delta \varnothing}{L}\right)_{Pt\ B} = T_{Pt\ B} \quad (37)$$

As equation (34) and (35) are related to E_1^* and t^*, the values satisfying two equations simultaneously can be found like Fig. 23.

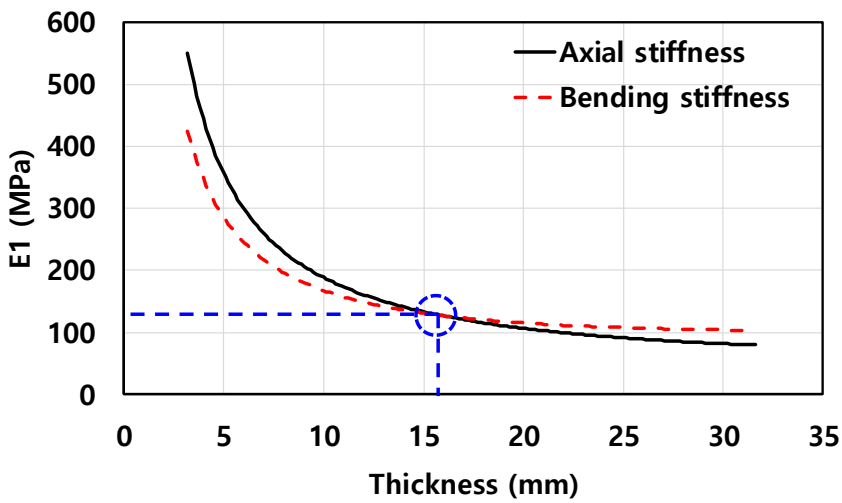

Fig. 23 Determination t^* and E_1^* using axial and bending stiffness

Then from the t^* and equation (36), E_2^* can be found. Likewise, from the t^* and equation (37), G_{12}^* can be found. As the result, the information of EQP is like Table 6.

Table 6 Material properties and geometric information of EQP

Layer	OD (mm)	t^* (mm)	E_1^* (GPa)	E_2^* (GPa)	G_{12}^* (GPa)	ν	Type of element	Type of Material
EQP	95.4	15.8	0.128	154.3	70.12	0.3	SHELL 181	Orthotropic shell

4.2.2. Verification of EQP

In the previous section, the EQP is determined by the analytical method. In this section, this layer is verified by the numerical method. At first, the layers of part B and EQP are made by FE models. Fig. 24 shows two FE models. Because the thickness of EQP is far larger than other layers, and deformation over the thickness cannot be ignored, this layer is modeled with solid elements. Next, elastic analyses about axial force, torsion, bending, and external pressure are examined based on two FE models. Table 7 shows the comparison of various values of stiffness of two FE models represented in Fig. 24. As a result, about all stiffness tests, two FE models show similar results shown in the following table. Therefore, EQP can replace the layers of part B. This layer is used for composing 5-layered model.

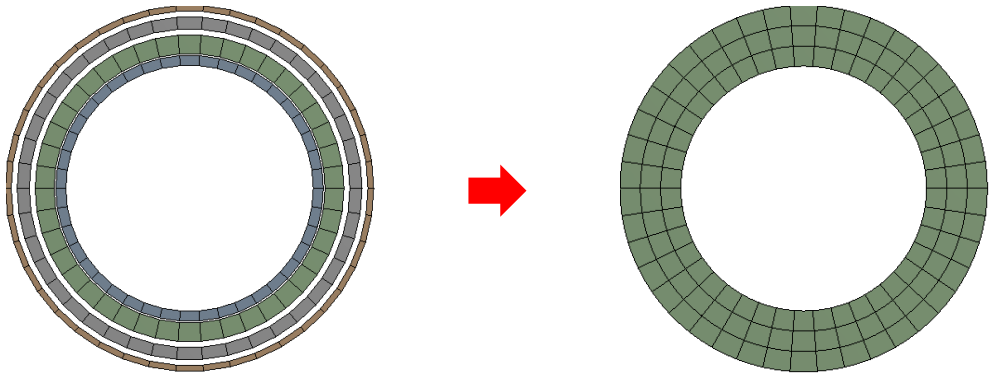

Fig. 24 FE models of part B layers (L) and EQP (R)

Table 7 Verification of equivalent pressure layer

	4-layered model	EQP model (error)
Axial stiffness (MN)	499.7	505.7 (1.2%)
Torsion stiffness (kNm2)	308.2	292.8 (5%)
Bending stiffness (MNmm2)	789	838 (5.8%)
Radial stiffness(kN/mm3)	1.5	1.59 (6%)

4.2.3.3D 5-layered Model

A model containing four layers of EQP and part A is called a 5-layered model. A pair of tensile armor layers is composed of 2-noded beam elements, and a pair of tape layers is modeled of 4-noded shell elements. However, EQP is composed of 8-noded solid elements because the thickness is very thick compared to other layers and thickness variation is not negligible. The remaining

contact and analysis conditions were set the same as for the 8-layered model. The Fig. 25 shows 5-layered FE model. In addition Table 8 and Table 9 represent the properties of elements and material and information of contact pairs in 5-layered model.

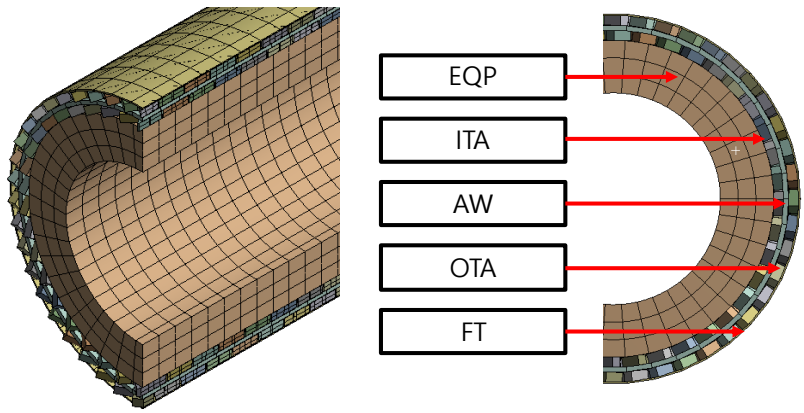

Fig. 25 5-layered FE model

Table 8 Elements and materials in the 5-layered model

No.	Layer	Type of element	Type of Material
1	EQP	SOLID185	Orthotropic
2	Tensile armor 1	BEAM188	Isotropic
3	Anti-friction tape	SHELL181	
4	Tensile armor 2	BEAM188	
5	Fabric tape	SHELL181	

Table 9 Information on contact pairs' elements and properties of 5-layered model

No.	Contact	Target	Elements	FTOL
1	Tensile armor 1	EQP	Conta175/ Targe170	Larger than 1%
2	Tensile armor 1	Anti-friction tape		
3	Tensile armor 2	Anti-friction tape		
4	Tensile armor 2	Fabric tape		

5. Verification of Model

5.1. Axial tension test

In this study, practical FE models are proposed. The FE models created from 'simplification of geometry' and 'isotropic assumption of tape layers' are called 8-layered models. Depending on the element type of the polymer layers, 8-layered models are divided into a solid model and a shell model. In addition, the FE model created through 'simplification of composition' is called a 5-layered model.

In this step, elastic analyses of the proposed FE models are performed. Axial stiffness and bending stiffness are calculated, and the models are verified by comparing with analytical methods and

experimental results. Here, several issues related to the numerical method are examined. First, 8-layered solid model and shell model are compared, and the effect of FTOL on the axial stiffness of the shell model is examined. Next, the validity of the isotropic assumption of tape layers is verified. Finally, the 8-layered model and the 5-layered model are compared.

5.1.1.Solid Model vs Shell Model

As described earlier ‘process of numerical method’, the polymer layers have a small elastic modulus compared to the metal layers, so they must be composed of solid elements because the thickness deformation cannot be ignored. However, somehow shell elements seem to be more suitable because their thickness are much smaller than radius. Therefore, two models of solid and shell model are proposed depending on the element type of polymer layers. The Fig. 26 shows the result of axial tension test. According to the figure, axial stiffness of shell model is about 25% larger than that of solid model.

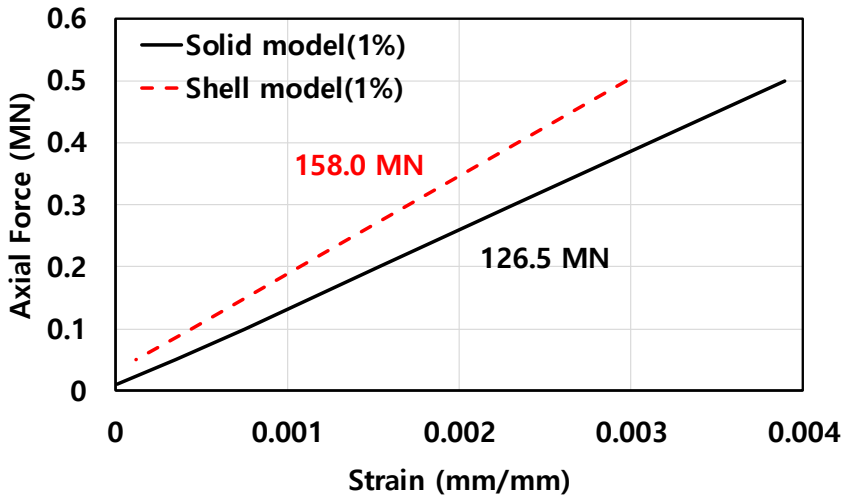

Fig. 26 Axial stiffness of solid and shell model

The reason of the difference is resulted from thickness changes of both elements due to contact between other elements. Solid element deforms when it contact with another element in thickness direction. Meanwhile, shell element defined as a virtual thickness keep the constant thickness without deformation, thus shell element is more rigid than solid elements when it makes contact with another element. Therefore, in the axial tension test where lots of contact between elements occurs, the shell model is likely to be stiffer. In this study, FTOL (factor of penetration tolerance) is proposed to solve the problem of shell element. The Fig. 27 represents the results of axial stiffness of shell models depending on the FTOL.

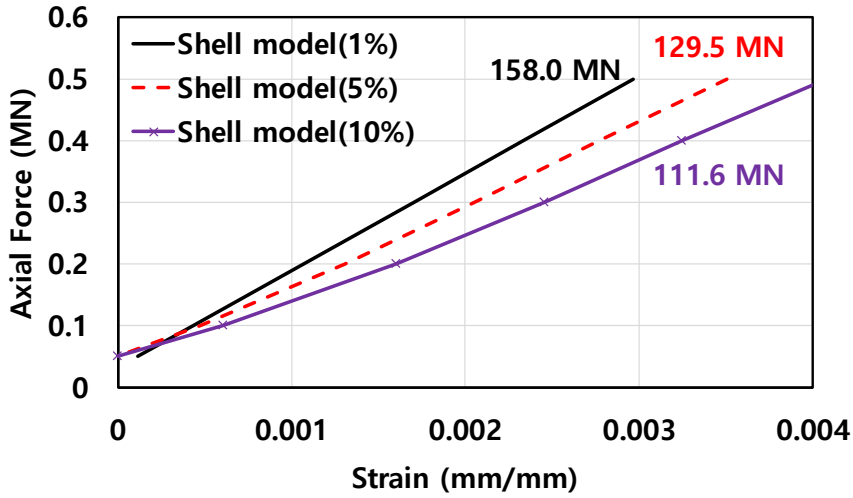

Fig. 27 The effects of FTOL on axial stiffness of shell model

Based on Case 1(FTOL 1%), the axial stiffness of Case 2(FTOL 5%) is about 18% smaller and the result of Case 3(FTOL 10%) is about 31% smaller. This results show that axial stiffness of shell model is very sensitive to FTOL.

For ANSYS guidance (R.15), FTOL of 1% of the element thickness is recommended. This value can guarantee both convergence and accuracy while minimizing penetration between elements that cannot be avoided in numerical analysis. This value can be used for solid elements. Then a question remains as to which FTOL should be used. In order to solve this question, in this study, analytical method is used. According to Bahtui et. al (2009), thickness changes of polymer layers can be obtained by the following

equations.

$$\Delta t_i = \Delta P_i \frac{(2-\nu_i){R_i}^2}{2E_i t_i} - \frac{\nu_i E_i R_i}{A_i E_i},\ i = 2,4,6,8 \quad (16)$$

$$u_{r.3} - u_{r.1} = \Delta t_2,\ u_{r.5} - u_{r.3} = \Delta t_4,\ u_{r.7} - u_{r.5} = \Delta t_6 \quad (17)$$

The analytical equations are used to determine the maximum value of the thickness changes of polymer layers in the axial tension test. For a very large axial tension, thickness changes of polymer layers are converged to some values. Thickness changes of pressure sheath and fabric tape are not large, and they are smaller than 1% of original thickness. However, thickness changes of inner anti-friction tape and outer anti-friction tape are converged to 2.2% and 4%, respectively. These values are put into the FTOL of shell model. The Fig. 28 shows the result of FTOL which is derived from analytical equations. This is compared with other results, which are solid model, experiment of Witz (1996), and analytical method of Bahtui et. al (2009).

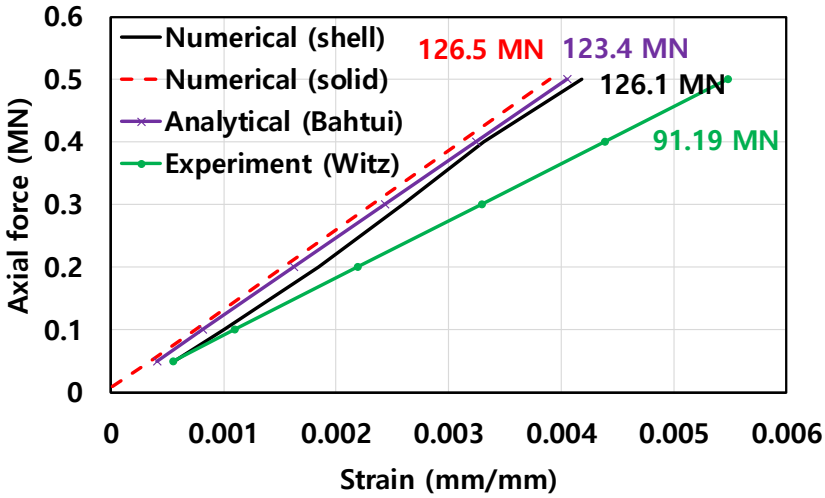

Fig. 28 Comparison of axial stiffness with reference methods

Although both the solid model and the shell model proposed in this study are reasonable, a shell model has been adopted for further study. In addition, according to Fig. 28, experimental result of Witz (1996) shows significantly different result from other results. Witz (1996) explained this is because of the unavoidable small errors in the measurement of axial elongation and unknown gaps between component layers.

5.1.2.Isotropic Assumption

The 8-layered model includes three tape layers (a pair of anti-friction tapes, fabric tape). These layers are orthotropic layers. However, in this study, these layers are considered as isotropic

layers due to the convergence problem.

Next, isotropic assumption is verified using elastic analyses. Tape layers have different modulus (E_1,E_2). Where subscribe 1 means axial direction, and subscribe 2 means transverse direction. In general, E_2 is larger than E_1. Then two isotropic layers can be considered. The first one (layer I) is isotropic having E_1 as its elastic modulus, and the other one (layer II) has E_2 as its elastic modulus. The Fig. 29 shows two isotropic and one orthotropic layer, and the relationships of axial stiffness of these layers. In the way all orthotropic tapes are related with layer I (E_1) and layer II (E_2). In addition, let 8-layered 'model I' have all layers I, and 'model II' have all layers II. Then axial stiffness of orthotropic model will be between those of model I and II.

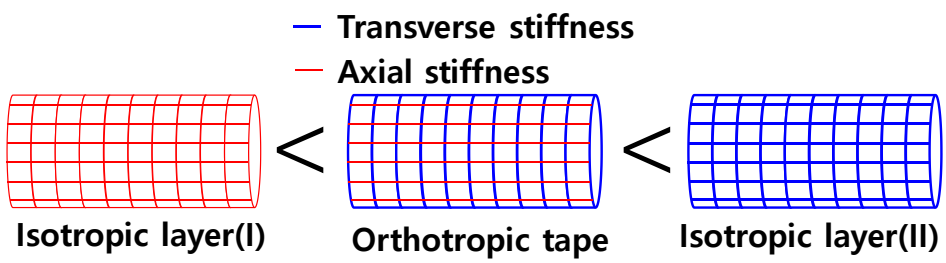

Fig. 29 Isotropic layers corresponding to orthotropic tape

The Fig. 30 shows the axial stiffness of model I and II. Elastic analysis shows that the axial stiffness of both isotropic models is

very similar. (0.7% of error)Therefore, the axial stiffness of the orthotropic model will be very similar to those of the isotropic models. As a result, the isotropic assumption proposed in this study is reasonable.

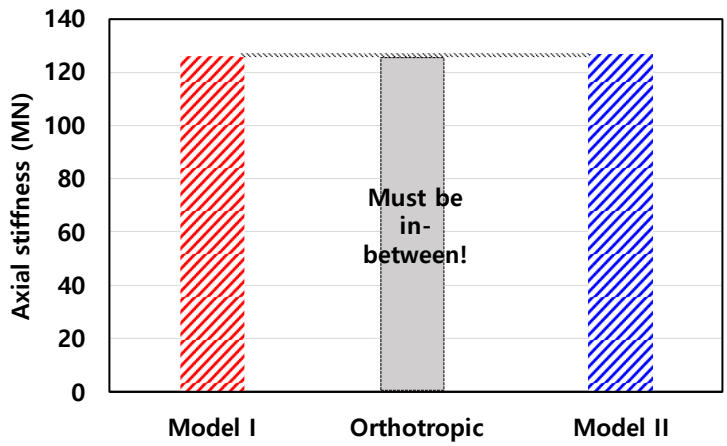

Fig. 30 Comparison of axial stiffness of two isotropic models

5.1.3.8-lyaered Model vs 5-layered Model

In this study, the method of simplification of composition is proposed. Depending on whether they have direct effects, 8 layers are divided into two parts: part A and part B. The layers of part A are closely related to radial buckling, and they are fabric tape, outer anti-friction tape, and a pairs of tensile armor layers. On the other hand, the layers of part B are not closely related to radial buckling, and they are carcass, pressure sheath, pressure armor, and inner

anti-friction tape. The role of the layers of part B is mainly to withstand pressure. Therefore, an EQP is proposed to replace these layers. The EQP is determined so that the behavior for various loads is equal to that of part B. Analytical method was used in this process and it was verified by FE model.

Next, the 5-layered model including the EQP can be validated by comparing axial stiffness and bending stiffness to the 8-layered model. Fig. 309 compares axial stiffness of two models and other reference methods. According to the

Fig. 31, the axial stiffness of the 5-layer model is 137.18 MN, which is similar to the axial stiffness of the 8-layer model (126.05 MN), and has an error of about 8.8%.

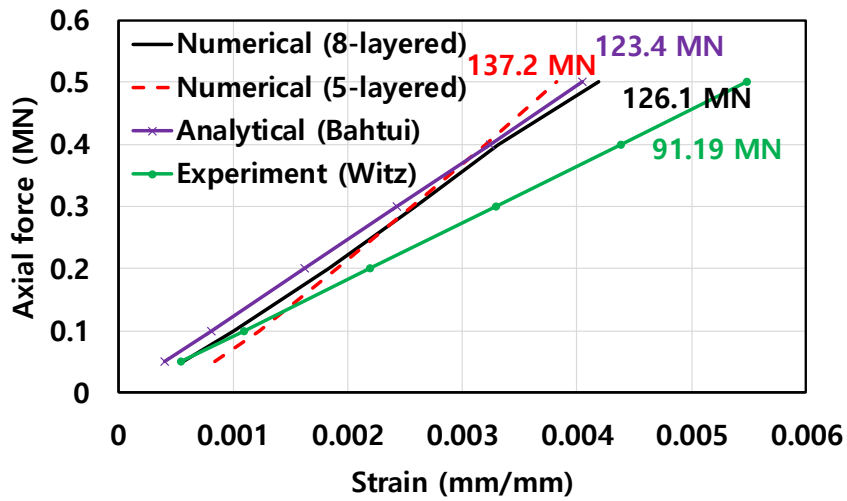

Fig. 31 Axial stiffness of two FE models and references

5.2. Bending Test

The bending stiffness of two FE models is calculated.

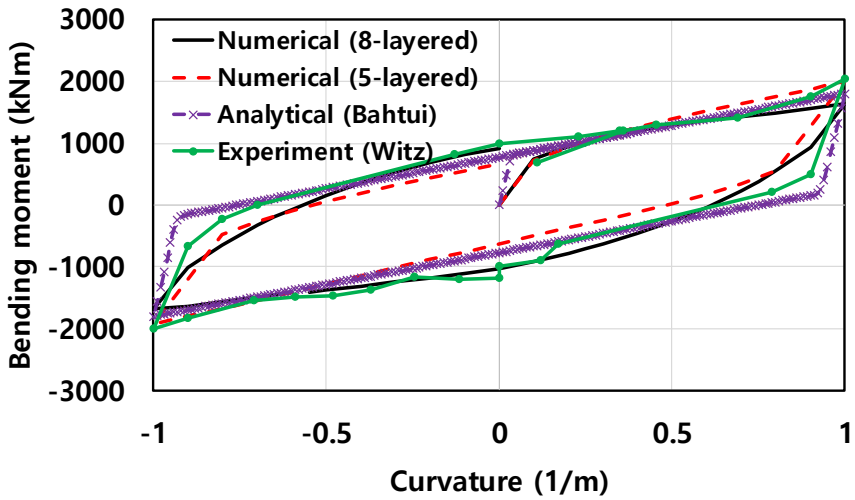

Fig. 32 Bending stiffness of two FE models and references

The condition of analyses is of the internal pressure of 30 MPa and the external pressure of 4 MPa, which was same with those of Witz (1996). The Fig. 32 shows the bending stiffness of two FE models and other reference methods.

6. Application to Ultimate Strength Analysis

6.1. Radial Buckling

The final goal of this study is to evaluate the ultimate compressive strength using practical FE methods. Because the 8-layered model

has so many layers that it could not converge stably, the 5-layered model is used for ultimate compressive strength.

The information of elements and contact pairs are represented in Table 8 and Table 9. Next, one end of the model is constrained for 6 degrees of freedom to prevent rigid body motion, and displacement condition is applied on the other end.

The Fig. 33 shows the relationship between axial compressive force and shortening amount. From the initial point to the point A, the axial compressive force and the shortening amount show a linear relationship. After point A, the slope of the graph increases. This means that the stiffness of the model against the axial compressive force is reduced. After the point D, the resistance of the model becomes 0 even for very small axial compressive force. On the other hand, the range of strains in which interlocking does not occur in the simplification of geometry of layers is explained. Carcass ranges from -5.6% to 4.5%, and pressure armor is from -6.7% to 6.7%. Therefore, interlocking does not occur within the scope of this interpretation. Therefore, the expression of Sousa (2005) can be used. Next, mechanisms by layers will be examined in detail.

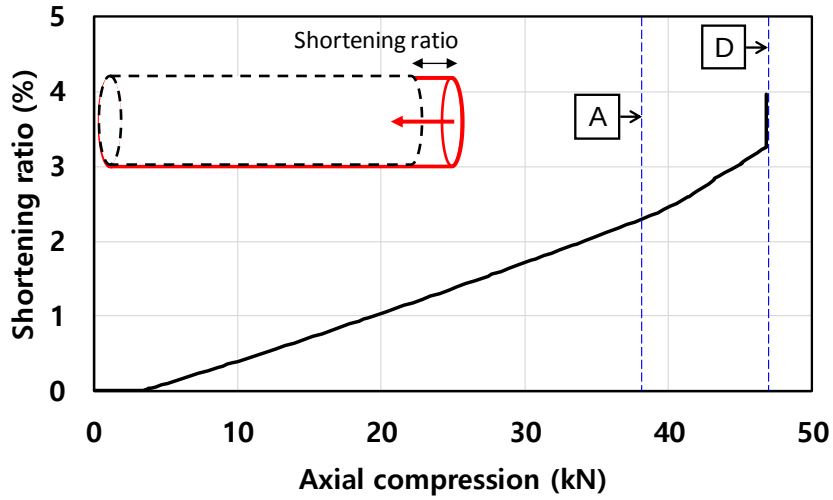

Fig. 33 Shortening ratio versus axial compression

The

Fig. 34 shows the relationships between the radial deformation and the axial compression of the layers of part A (one pair of tensile armor and one pair of tape layers) which are related to the failure mechanism directly.

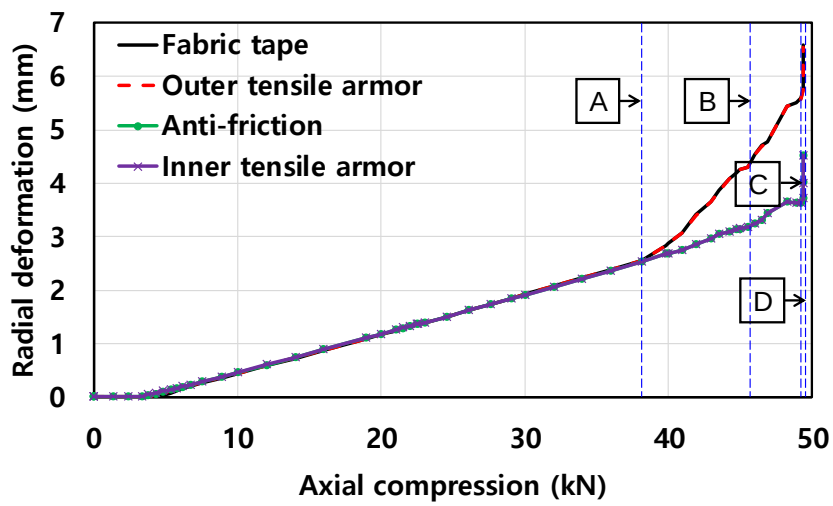

Fig. 34 Radial deformation versus axial compression

The interesting thing is that the tensile armor and the tape layer move together in pairs. In other words, the inner tensile armor and the anti-friction tape move in pair, and the outer tensile armor and fabric tape move together like the Fig. 35.

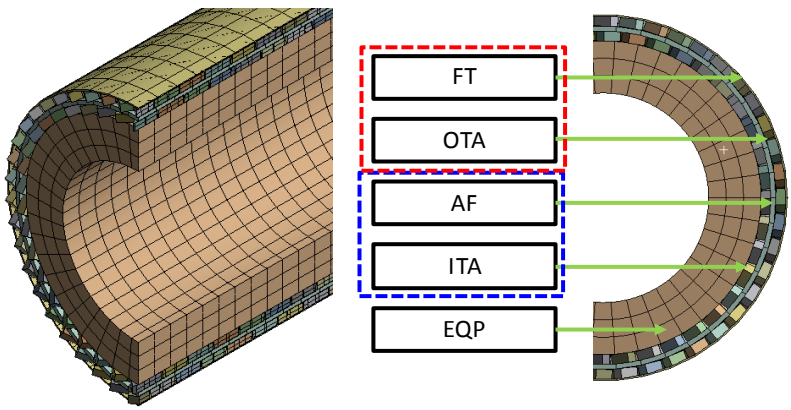

Fig. 35 Two pairs of layers moving together

According to the

Fig. 34, from the beginning to A point, four layers expand together. However, from the point A, a gap between the two pairs occurs. This gap gets larger and larger at point D. The numerical analysis ended at point D because a large displacement occurs instantaneously at point D.

Next, the radial can be explained with the relations between the stress and the axial compression like the Fig. 36. From the beginning to the point A, the stress of the tape layer increases

linearly due to the contact pressure with tensile armor. At point A the stress of the fabric tape becomes the yield strength.

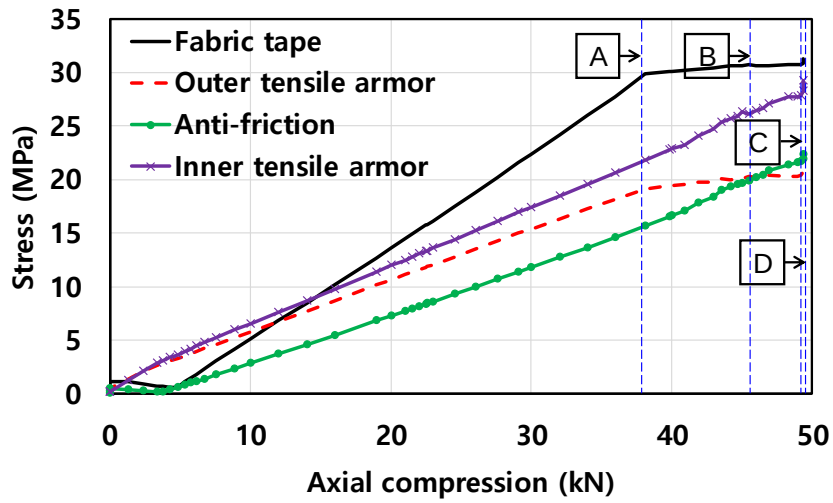

Fig. 36 Maximum equivalent stress versus axial compression

Saevik (2012) called the point A radial buckling point. However, the model of Saevik (2012) did not reflect plastic deformation. In this research, there is a post-buckling region (from A to D). At point B, the stress of the anti-friction tape becomes the yield stress. In addition, at point C and D, the stresses of anti-friction tape and fabric tape become tensile strength, respectively. After point D, the model loses its resistance to very small axial compression. Therefore, the point D can be called the ultimate compressive strength. As a result, the ultimate compressive strength of the model is closely related to the material properties of

the tape layers due to the failure mechanism.

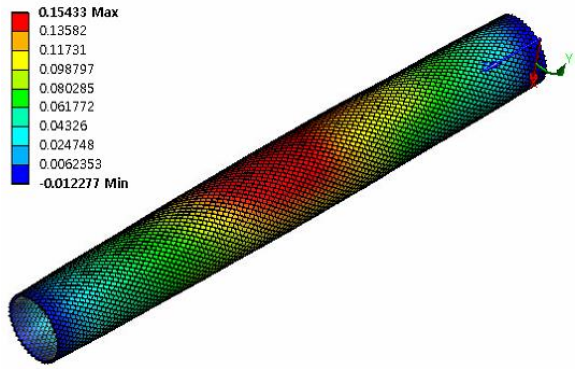

Fig. 37 The radial deformation of outer tensile armor at ultimate compressive strength

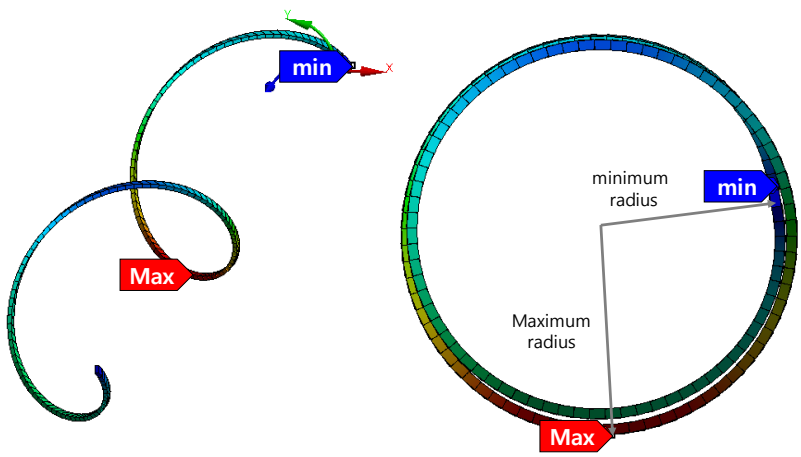

Fig. 38 The radial deformation of a tendon of outer tensile armor at ultimate compressive strength

The Fig. 37 and Fig. 38 represent the radial deformation of outer tensile armor at ultimate compressive strength. Since the analysis of ANSYS Mechanical cannot converge at the moment of large

deflectionm, the shape of extreme swelling cannot be identified. However, it is certainly found that the radial deformation at the center is the largest. Moreover, Fig. 39 shows the stress of fabric tape at ultimate compressive strength. The stress of large part including center reaches its yield strength.

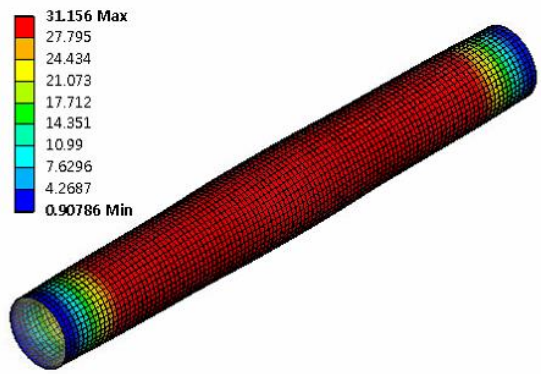

Fig. 39 Max. Equivalent stress of fabric tape at ultimate compressive strength

In order to verify the validity of numerical method, the results are compared with analytical method of Saevik (2012). The equations below show the relationship between the axial stress of tendon and stress of tape layer.

$$\sigma_{tape} = \frac{R_{tape}}{t_{tape}} p_t = \frac{R_{tape}}{t_{tape}} \frac{n\sigma_a A \cos\alpha \tan^2\alpha}{2\pi R_{TA}^2} = \sigma_Y \qquad (30)$$

$$\sigma_{a.buckling} = \frac{t_{tape}}{R_{tape}} \frac{2\pi R_{TA}^2}{nAcos\alpha\, tan^2\alpha} \sigma_Y \qquad (30-a)$$

Using these equations, at the radial buckling point, the axial stress of the tensile armor becomes 15.4 MPa, and the corresponding axial compression force is 41.4 kN.

On the other hand, the Fig. 40 shows the relationship of stresses between fabric tape and outer tensile armor. Radial buckling point depends on the yield strength of tape (30 MPa) so the line 1 can be drawn. From the intersection between line 1 and fabric tape curve, vertical line 2 can be drawn. Next, from the intersection between line 2 and outer tensile armor curve, the stress of tensile armor at the radial buckling point can be found. According to the Fig. 40, the stress of tensile armor at the radial buckling point is 17.4 MPa, and the corresponding axial compression force is 38 kN. They are very similar to analytical results. Therefore, it can be concluded that the solution obtained from numerical analysis is valid.

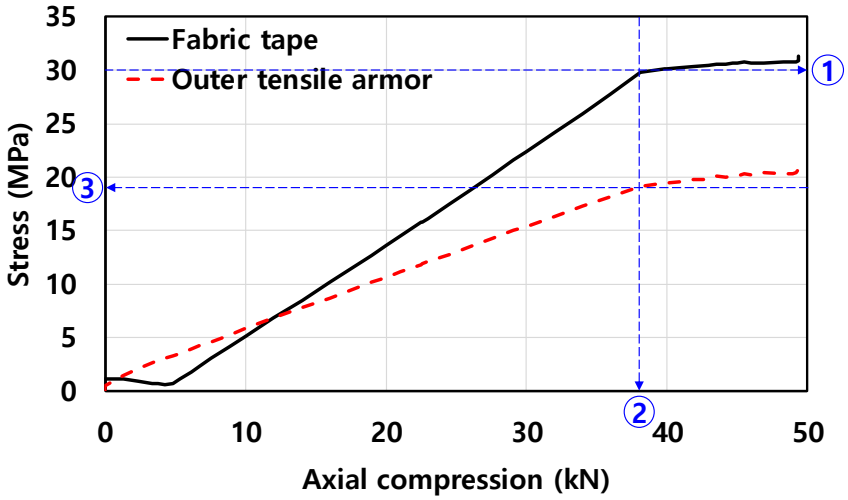

Fig. 40 Relationship of stresses between tape and tensile armor

Additionally, case studies are conducted with various yield strength, thickness, and elastic modulus of tapes. According to Saevik (2012), it can be predicted that radial buckling point is proportional to the yield strength and thickness of the tape. However, it seems to be independent to the elastic modulus of the tape.

$$\sigma_{a.buckling} = \frac{t_{tape}}{R_{tape}} \frac{2\pi R_{TA}^2}{nA\cos\alpha \tan^2\alpha} \sigma_Y \qquad (30-1)$$

In this research, numerical analyses are performed to examine the influences of various parameters. Fig. 41~Fig. 43 show the results of analytical and numerical methods.

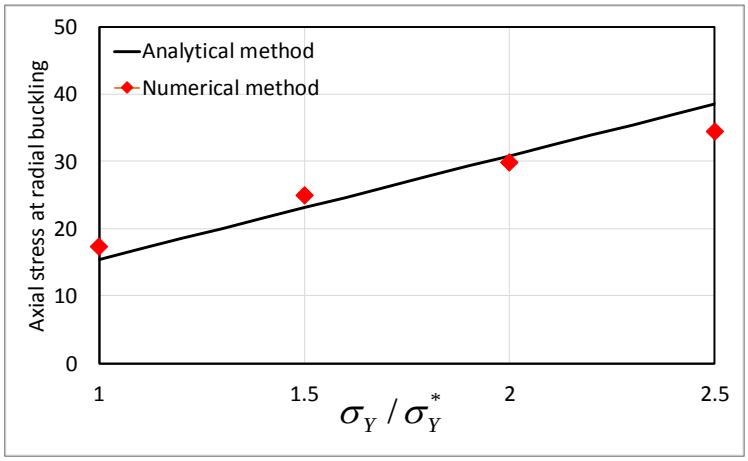

Fig. 41 The influence of yield strength on the stress of TA

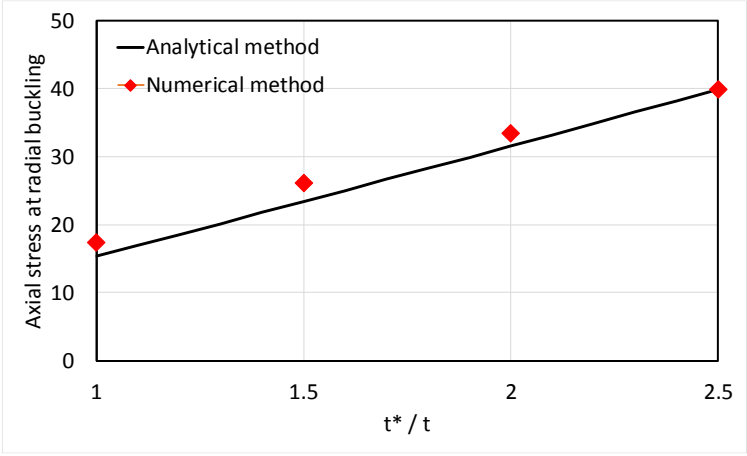

Fig. 42 The influence of thickness on the stress of TA

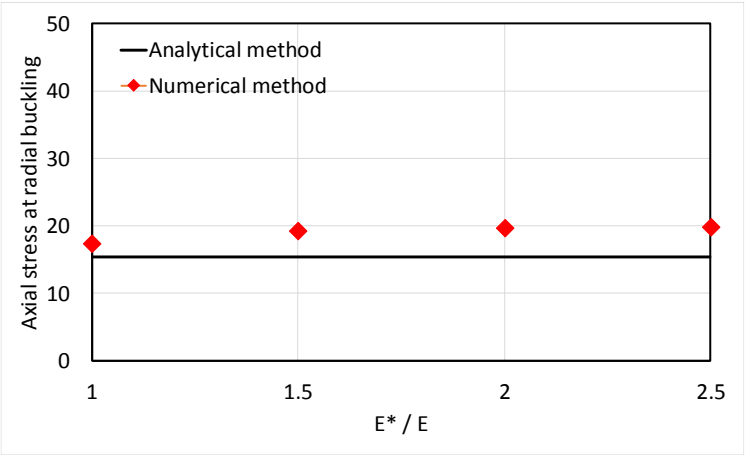

Fig. 43 The influence of elastic modulus on the stress of TA

Next, the effect of ovalization on the ultimate compressive strength is examined. Ovalization means the degree of distortion of circle like the Fig. 44.

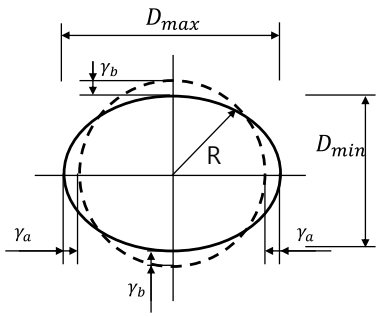

Fig. 44 Definition of ovalization

The Fig. 45 and Fig. 46 below show the radial deformation and the axial stress of tensile armor layers for various ovalization. According to the Fig. 45, the larger the ovalization is, the faster the tensile armor layers expand. However, ovalizaion does not seem to

be related to the stress of tensile armor layers. In addition, there is no effect of ovalization on radial buckling point and ultimate strength.

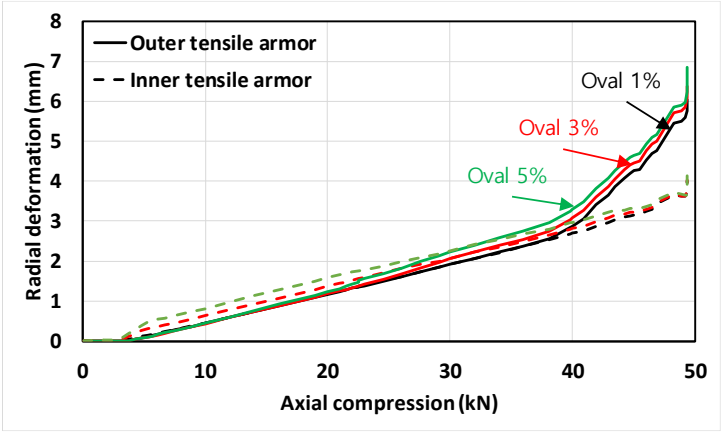

Fig. 45 Radial deformation of tensile armors versus axial compression of different ovalization

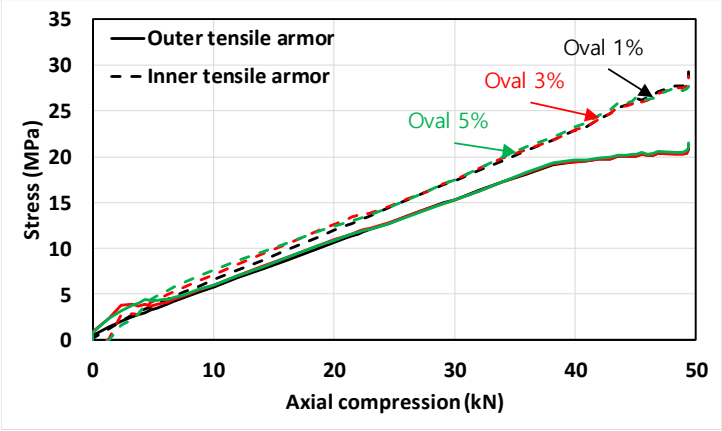

Fig. 46 Max. Equivalent stress of tensile armor layers versus axial compression of different ovalization

Finally, the effect of external pressure on the ultimate compressive strength is examined. The Fig. 47 and Fig. 48

represent the radial deformation of tensile armor layer and the stress of tape layer for various external pressures.

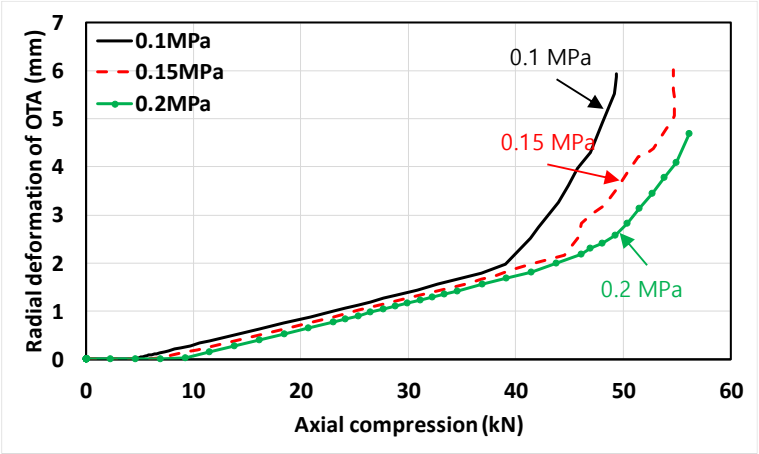

Fig. 47 Radial deformation of outer tensile armor versus axial compression of different external pressure

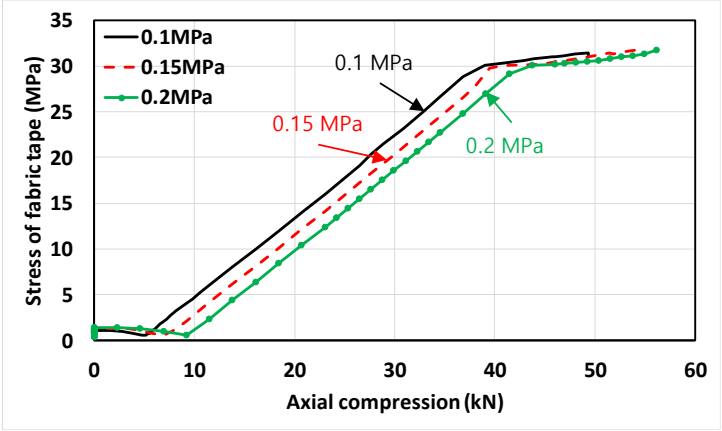

Fig. 48 Max. Equivalent stress of fabric tape versus axial compression of different external pressure

As the result, the larger the external pressure is, the bigger the

radial buckling point and the ultimate compressive strength are. This is because the external pressure and the axial compression have opposite effects on the behavior of the tendon.

7. Conclusion

This paper proposes practical FE analysis methods for ultimate-strength assessment based on practical numerical method and reasonable assumptions. Three steps of simplification are used: simplification of geometry of layers, isotropic assumption, and simplification of composition of model. An 8-layered FE model and a 5-layered FE model were generated through a series of processes. These models are validated through elastic analysis. Results were compared with analytical method and experimental results. In this process, the effect of FTOL on the axial stiffness of the shell element and the validity of the isotropic assumption were verified.

On the other hand, in the case of ultimate compressive strength analysis, the 8-layered model including all layers is hard to converge due to its high non-linearity. In order to simplify the complicated interactions between layers, the inner 4 layers (carcass, pressure sheath, pressure armor, and inner anti-friction

tape) are replaced with an equivalent pressure layer (EQP). The EQP has the same behavior for the 4 layers inside and the axisymmetric load and bending moment. The analytical method was used in this process.

In the ultimate compressive strength analysis, the strengths of the polymeric layers that are wrapped around the tensile armor layers are critical, because radial expansion of the tensile armor layers follows failure of polymer layers. After the polymer layers arrive at their yield strengths, tensile armor layers swell up rapidly. This point is a radial buckling. Due to the effect of plastic deformation, ultimate compressive strength is larger than radial buckling point. The stress and overall axial compression of the tensile armor at the radial buckling point were verified by comparing it with the equation of Saevik (2012). The material properties and geometric information of the tape were changed and the case study was carried out. Whereas ovalization effects different sensitivities of radial deformation to compression, it is negligible with respect to ultimate compressive strength. In addition, the larger the external pressure is, the greater the radial buckling point and the ultimate compressive strength are. This is because external pressure has an opposite effect to axial compression.

Reference

[1] ANSYS, 2013. Mechanical APDL Documentation, R15.0. SAS IP, Inc.

[2] Handbook on Design and Operation of Flexible Pipes, 2014. Vol.1, MARINTEK / NTNU / 4Subsea

[3] American Petroleum Institute (API), 2002. API RP 17B, Recommended Practice for Flexible Pipe, 3rd Ed.

[4] Feret, J.J. and Bournazel, C.L., 1987. Calculation of Stresses and Slip in Structural Laters of Unbonnded Flexible Pipes, Journal of Offshore Mechanics and Arctic Engineering, Vol.109, pp263-269.

[5] McNamara, J.F. Harte, A.M., 1992. Three-Dimensional Analytical Simulation of Flexible Pipe Wall Structure, Journal of Offshore Mechanics and Arctic Engineering, Vol.114, pp69-75

[6] Witz, 1996, A Case Study in the Cross-section Analysis of Flexible Risers, Marine Structures 9, pp885-904.

[7] Kebadze, R, 2000. Theoretical Modeling of Unbonded Flexible Pipe Cross-Sections, Degree of Doctor of Philosophy, South Bank University, UK.

[8] Bahtui, A., Bahai, H. and Alfano, G., 2009. Numerical and analytical modeling of unbounded flexible risers, Journal of Offshore Mechanics and Arctic Engineering, Vol.131, No.021401.

[9] Sousa, J.R.M., Magluta, C. Roitman, N., Ellwanger, G.B. and Lima E.C.P. 2009. On the response of flexible risers to loads imposed by hydraulic collars, Applied Ocean Research, Vol.31, pp157-170

[10] Sousa, J.R.M., Viero, P.F., Magluta, C. and Roitman, N., 2012. An Experimental and Numerical Study on the Axial Compression Response of Flexible Pipes, Journal of Offshore Mechanics and Arctic

[11] Vaz, M.A., Rizzo, N.A.S., 2011. A Finite Element Model for Flexible Pipe Armor Wire Instability, Marine Structures 24 (2011) pp 275-291

[12] Saevik S., Torsen M.J., 2012. Techniques for predicting tensile armor buckling and fatigue in deep water flexible risers, Proceeding of the ASME 2012 31st International Conference on Ocean, Offshore and Arctic Engineering, July 1-6, 2012, Rio de Janeiro, Brazil

[13] I., Kraincanic, E., Kebadze, 2001, Slip initiation and progression in helical armouring layers of unbonded flexible pipes and its effect on pipe bending behaviour, Journal of Strain Analysis VOL 36 NO 3

[14] Sousa, J.R.M. 2005. Local analysis of flexible risers through the finite element method, D.SC. Thesis, COPPE/URFJ.

[15] Saevik, S. and Berge, S., 1995. Fatigue testing and theoretical studies of two 4 inch flexible pipes, Engineering Structures. Vol. 17, No.4, pp.276-292.

초록

축 압축력을 받는 유연식 라이저의 극한 강도의 간략화 모델을 이용한 유한요소 해석

유연식 라이저는 해저 플랫폼과 해저 플로우 라인을 연결하고 가스와 오일을 이송하는 파이프이다. 유연식 라이저는 설치 및 작동 과정에서 많은 불확실한 요소를 접할 수 있다. 특히, 설치 공정 중에, 압력 불균형으로 인해 유연식 라이저는 원치 않는 힘인, 축 방향 압축을 받을 수 있다. 축 방향 압축은 반지름 방향의 좌굴과 같은 실패 모드를 초래할 수 있다. 따라서 실패 모드를 분석하고 유연식 라이저의 극한 압축 강도를 평가하는 것이 매우 필요하다. 유연식 라이저의 극한 강도 평가는 매우 복잡하고 많은 시간이 든다. 왜냐하면 재료의 비선형성, 대변형 및 비선형 접촉 메커니즘과 같은 다양한 구조적 난점을 포함하기 때문이다. 이 논문은 간략한 FE 모델을 사용하여 극한 강도 평가를 위한 실용적이고 안정적인 방법을 소개한다. 우선 레이어의 단면 모양을 간략화하고, 테이프를 등가레이어로 치환하고, 실패 매커니즘을 이해하여 모델의 구성을 간략화한다. 모델의 구성을 간략화 하기 위해서는 수치 해석적 방법이 사용된다. 생성한 FE 모델의 타당성을 검증하기 위해 탄성해석을 통해 축 강성 및 굽힘 강성을 구하고, 이를 참조 결과들과 비교한다. 또한 본 논문의 최종 목표인 극한 강도 해석을 수행한다. 이후 테이프 레이어의 물성치 및 기하학적 정보가 극한 압축

강도에 미치는 영향을 케이스 스터디를 통해 알아보고, ovalization 및 외압이 극한 압축 강도에 미치는 영향을 살펴본다.

주요어 : flexible risers, ultimate strength assessment, failure mode, nonlinear FE analysis, simplified FE models

학 번 : 2015-22866